Original Article

Hemodynamic property incorporated brain tumor segmentation by deep learning and density-based analysis of dynamic susceptibility contrast-enhanced magnetic resonance imaging (MRI)

Leonardo Tang[1], Tianhe Wu[1], Ranliang Hu[1], Quanquan Gu[1], Xiaofeng Yang[2], Hui Mao[1]

[1]Department of Radiology and Imaging Sciences, Emory University School of Medicine, Atlanta, GA, USA; [2]Department of Radiation Oncology, Emory University School of Medicine, Atlanta, GA, USA

Contributions: (I) Conception and design: All authors; (II) Administrative support: R Hu, X Yang, H Mao; (III) Provision of study materials or patients: L Tang, T Wu, Q Gu, R Hu, H Mao; (IV) Collection and assembly of data: L Tang, T Wu, Q Gu, H Mao; (V) Data analysis and interpretation: All authors; (VI) Manuscript writing: All authors; (VII) Final approval of manuscript: All authors.

Correspondence to: Hui Mao, PhD. Department of Radiology and Imaging Sciences, Emory University School of Medicine, 1750 Haygood Drive, Atlanta, GA 30322, USA. Email: hmao@emory.edu.

Background: Magnetic resonance imaging (MRI) is a primary non-invasive imaging modality for tumor segmentation, leveraging its exceptional soft tissue contrast and high resolution. Current segmentation methods typically focus on structural MRI, such as T_1-weighted post-contrast-enhanced or fluid-attenuated inversion recovery (FLAIR) sequences. However, these methods overlook the blood perfusion and hemodynamic properties of tumors, readily derived from dynamic susceptibility contrast (DSC) enhanced MRI. This study introduces a novel hybrid method combining density-based analysis of hemodynamic properties in time-dependent perfusion imaging with deep learning spatial segmentation techniques to enhance tumor segmentation.

Methods: First, a U-Net convolutional neural network (CNN) is employed on structural images to delineate a region of interest (ROI). Subsequently, Hierarchical Density-Based Scans (HDBScan) are employed within the ROI to augment segmentation by exploring intratumoral hemodynamic heterogeneity through the investigation of tumor time course profiles unveiled in DSC MRI.

Results: The approach was tested and evaluated using a cohort of 513 patients from the open-source University of Pennsylvania glioblastoma database (UPENN-GBM) dataset, achieving a 74.83% Intersection over Union (IoU) score when compared to structural-only segmentation. The algorithm also exhibited increased precision and localized predictions of heightened segmentation boundary complexity, resulting in a 146.92% increase in contour complexity (ICC) compared to the reference standard provided by the UPENN-GBM dataset. Importantly, segmenting tumors with the developed new approach uncovered a negative correlation of the tumor volume with the scores in the Karnofsky Performance Scale (KPS) clinically used for assessing the functional status of patients (–0.309), which is not observed with the prevailing segmentation standard.

Conclusions: This work demonstrated that including hemodynamic properties of tissues from DSC MRI can improve existing structural or morphological feature-based tumor segmentation techniques with additional information on tumor biology and physiology. This approach can also be applied to other clinical indications that use perfusion MRI for diagnosis or treatment monitoring.

Keywords: Brain tumor; segmentation; dynamic susceptibility contrast (DSC); perfusion magnetic resonance imaging (perfusion MRI); deep learning

Submitted Oct 26, 2023. Accepted for publication Feb 04, 2024. Published online Mar 28, 2024.
doi: 10.21037/qims-23-1471
View this article at: https://dx.doi.org/10.21037/qims-23-1471

Introduction

Magnetic resonance imaging (MRI) offers superb resolution and exquisite soft tissue contrast for delineating tumors and lesions. Segmentation of tumors from magnetic resonance images is an essential process to derive quantitative information that can be used for diagnosis, tumor classification, and treatment monitoring (1). Most tumor segmentation approaches are based on the spatial information and signal intensity or contrast highlighted in images obtained with different MRI data acquisition sequences (2), which provide specific tissue contrast based on their unique MRI properties, such as longitudinal T_1 and transverse T_2 relaxation times and magnetic susceptibility. Typically, T_1 or T_2 weighted MRI sequences and a fluid-attenuated inversion recovery (FLAIR) sequence with additional gadolinium (Gd) contrast-enhanced T_1-weighted imaging are used in the clinical protocol to image brain tumors. Based on the corresponding contrast of a tumor appearing in these different MRI methods in comparison to the normal tissues, segmentation of tumors can be performed using various signal processing approaches, including most state-of-the-art deep learning networks (3,4). For example, convolutional neural networks (CNN) are typically used to perform recognition tasks in images by learning complex features of tumors to define tumor regions for segmentation in MRI (5). Architectures that have found success include U-Net, V-Net, and Attention U-Net, which enable tumor segmentation in a wide variety of anatomical structures, including the brain, liver, lung, and breast (6-9). However, the majority of current tumor segmentation approaches, if not all, are mostly based on morphological images and image features to determine the boundary and volume of a tumor (10). More recently, radiomics features obtained from morphological images are used to detail subtle differences in tumor tissues and intra-tumor heterogeneity to improve the segmentation (11-13). Nevertheless, segmentation results with those methods are mostly dependent on spatial information captured in the structural MRI scans. Importantly, physiological information of tumors, especially hemodynamic properties of the tumor revealed by dynamic susceptibility contrast (DSC) enhanced MRI, is completely overlooked. DSC MRI is commonly used in brain tumor imaging to record a four-dimensional (4D) dataset with an additional temporal dimension for capturing the blood supply to different regions of the tumor (14,15). Hemodynamic parameters of the tumor and normal tissue, including blood volume and blood flow, can be derived and calculated from the time-dependent signal changes when the intravenously injected bolus of the MRI contrast agent, typically a Gd-based contrast agent, is passing through the tumor vasculature (16). Therefore, DSC MRI provides important and quantifiable hemodynamic properties of tumor tissue that is more sensitive to tumor progression, recurrence, and treatment responses than structural and morphological MRI (14). For example, a significant increase in blood flow is indicative of the progression of a tumor that is likely driven by angiogenesis, as the formation of new blood vessels is essential to sustain the metabolic requirements of the tumor (17). Clinically, DSC perfusion MRI has been increasingly used for diagnosis and monitoring of glioblastoma (GBM), which is the most common class of malignant brain tumors (18,19). Previous investigations have consistently demonstrated a positive correlation between elevated relative cerebral blood flow (rCBF) and higher grades of gliomas (20,21). Furthermore, blood vessels in GBM are distorted, evidenced by traits such as incomplete basement membranes, irregular diameters, increased permeability, and tortuous branching patterns in the vasculature (22). GBM are extremely aggressive brain tumors characterized by heterogeneous components, including hemorrhage, ischemia, gelatinous regions, and necrosis, leading to diverse enhancement patterns (23,24). Thus, DSC perfusion MRI offers tumor tissue hemodynamic information to differentiate such heterogeneity (25,26). Clearly, conventional approaches of segmenting tumors solely based on morphological and structural images, such as T_1-weighted, T_2-weighted, and FLAIR images, are unable to capture the hemodynamic features when differentiating tumor tissues from others.

The current study attempts to include tissue hemodynamic properties derived from time-dependent DSC MRI data into tumor segmentation processes to "tag" the segmented tumor tissue with physiological information that is better correlated with tumor biology and pathology. As such, we developed a new method taking advantage of

both deep learning spatial segmentation techniques and hemodynamic information from perfusion MRI. By utilizing a density-based machine learning approach to analyze the DSC MRI time course profiles within a region of interest (ROI) segmented by a deep neural network, we can use the information captured by 4D DSC perfusion MRI data to further improve tumor segmentation for more accurately monitoring tumor progression and treatment responses.

Methods

We acquired MRI data from a cohort of 513 GBM patients in the University of Pennsylvania glioblastoma database (UPENN-GBM). Because of retrospective use of de-identified data from this open source available through the Cancer Imaging Archive (TCIA) at the National Cancer Institute (27-29), obtaining written informed consent from subjects was done at the original study site and not required for this study. All individuals in this database had been diagnosed with high-grade GBM and scanned at the University of Pennsylvania Health System between 2006 and 2018. Table S1 summarizes demographic and clinical information on these patients. We also selected a subset of 54 patients who had both pre-treatment scores of the Karnofsky Performance Scale (KPS), which measures neurological functions of the patients, and survival time after the 1st tumor resection. Other clinical data, including partial or total tumor resection, isocitrate dehydrogenase 1 (IDH1) mutation status, methylguanine-DNA methyltransferase (MGMT) promoter methylation status, and predicted pseudo-progression index, were too sparse in the selected cohort of these 54 patients, thus lacking sample size and power for appropriate correlation analysis. In the deep learning analysis of the cohort of 513 patients, the test set contained the specified subset of 54 patients, while the remaining 459 patients were randomly allocated to adhere to an overall 80–20 training-test split. The study was conducted in accordance with the Declaration of Helsinki (as revised in 2013).

All MRI data were obtained prior to surgery using 3T MRI scanners manufactured by various companies, including Siemens (Tim/Trio, Verio, SkyraFit, MAGNETOM Vida, Numaris 4, Trio, Espree, and AvantoFit) as well as GE (Signa Discovery MR 750). Image acquisition followed the standard clinical brain tumor protocol, encompassing T_1 and T_2 spin echo imaging, T_2 FLAIR, post-contrast T_1 spin echo imaging, and DSC MRI scans. Detailed information about the specific scanners and scan parameters is available in Table S2.

We preprocessed data according to a standardized image preprocessing protocol as used by UPENN-GBM, encompassing the preprocessing of both three-dimensional (3D) structural images and 4D DSC perfusion MRI data. The images were skull-stripped, resampled to the 1-mm isotropic resolution, and diffeomorphically co-registered to the SRI24 normal adult brain atlas (30) to ensure uniform image dimension and voxel size across images collected with different acquisition sequences.

Workflow

As illustrated in *Figure 1*, our tumor segmentation workflow entails a multi-step process. The overall algorithm can be interpreted in two main sections: first, applying supervised machine learning techniques on structural 3D MRI data, followed by incorporating 4D perfusion data using unsupervised machine learning techniques. Data samples for the proposed algorithm are available upon request.

Initially, we performed tumor segmentation on T_2 FLAIR images from 513 patients (*Figure 1A*) employing a Keras-based implementation of the U-Net CNN (3). This U-Net variant was meticulously trained to identify tumor regions specifically from T_2 FLAIR images (*Figure 1B*) and generated a segmentation mask (*Figure 1C*) that was then co-registered using diffeomorphic co-registration to time-course images from DSC MRI (*Figure 1D*) to ensure that the tumor regions identified by the U-Net network on the T_2 FLAIR images were accurately located within the images collected with DSC MRI.

Upon establishing a ROI within the DSC MRI data, we proceeded to analyze and refine the tumor region, leveraging the temporal information embedded within the DSC MRI data using the Hierarchical Density-Based Scan (HDBScan) algorithm, a data-driven, density-based clustering method that is used to cluster data points within a collection based on a selected distance metric (9). In this experiment, each data point corresponded to a time course profile with 45 time-steps originating from individual voxels within the ROI in DSC MRI images. To optimize for computational efficiency without compromising data integrity, we applied dimensional reduction through principal component analysis (PCA) using the SciKit-Learn library (31), reducing the number of time steps per data point to 3–6 steps per data point by projecting each of 45 data points onto a lower coordinate basis while preserving >97% data variance (*Figure 1E*). Subsequently,

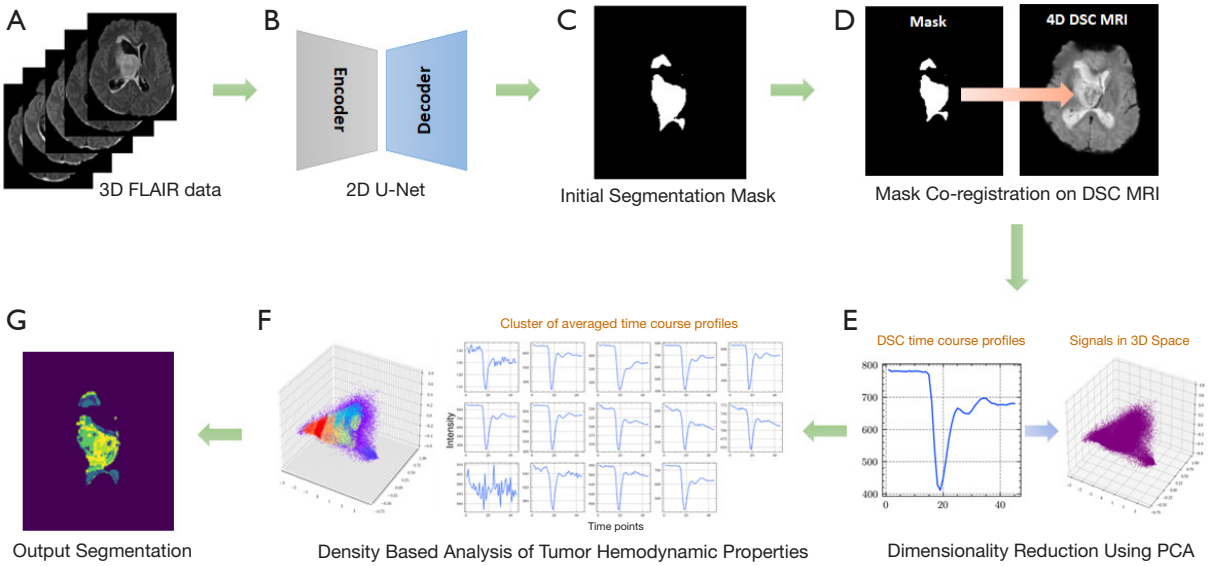

Figure 1 Overview of the algorithm workflow. (A) FLAIR images with tumors enhanced were used as input. (B,C) Initial tumor segmentation performed on structural data with 2D U-Net to generate the tumor mask (or ROIs) in each slice. (D) Diffeomorphic co-registration of ROI onto DSC perfusion MRI data. (E) Dimensionality reduction of DSC perfusion MRI data along time points dimension using PCA. (F) Density-based analysis of hemodynamics in resulting low-dimensional form of DSC perfusion MRI data within ROI. (G) Output segmentation after density-based analysis. 3D, three-dimensional; FLAIR, fluid-attenuated inversion recovery; 2D, two-dimensional; 4D, four-dimensional; DSC, dynamic susceptibility contrast; MRI, magnetic resonance imaging; PCA, principal component analysis; ROI, region of interest.

using the HDBScan Python library (32), we conducted two HDBScan passes on this lower coordinate basis: the first using the Excess of Mass (EOM) method and Euclidean distance for cohesive and optimal clusters, and the second using the Leaf method and Euclidean distance for finer clustering (*Figure 1F*). To harmonize the outcomes of these two passes, we synthesized a new cluster by constructing cluster centroids derived from the Leaf pass of HDBScan, which established the number of clusters in the final segmentation. Data points were assigned to these resulting clusters using a nearest-neighbor algorithm, drawing from the EOM pass of HDBScan. This integration approach unified the strengths of both passes, enhancing precision by removing the outliers identified during cluster generation. It also ensured that the resulting segmentation reflects the true tumor region according to the hemodynamically active tissue informed by DSC perfusion MRI data (*Figure 1G*).

U-Net model

We used a CNN-based U-Net architecture to make up the structural segmentation backbone of our algorithm. *Figure 2* presents the model that uses the standard encoder-decoder framework with skip connections between the corresponding feature maps of the encoder and decoder layers (6). The encoder network consists of convolutional layers in tandem with pooling operations to extract hierarchical features from the input image and output a latent feature representation. The decoder network up-samples this latent feature representation and utilizes the skip connections to combine the up-sampled features with the corresponding hierarchical features collected from the encoder network to output the backbone segmentation. We implemented this modified two-dimensional (2D) U-Net to segment each axial slice image through the entire 3D volume and then employ conventional multi-planar reconstruction to form a 3D segmentation mask of the target volume. Training was performed using the Adam optimizer and categorical cross-entropy loss (33). Intermediate evaluation of the accuracy of the segmentation output was done and presented using the Dice coefficient.

Density-based analysis

Upon identifying the ROI output by the proposed U-Net

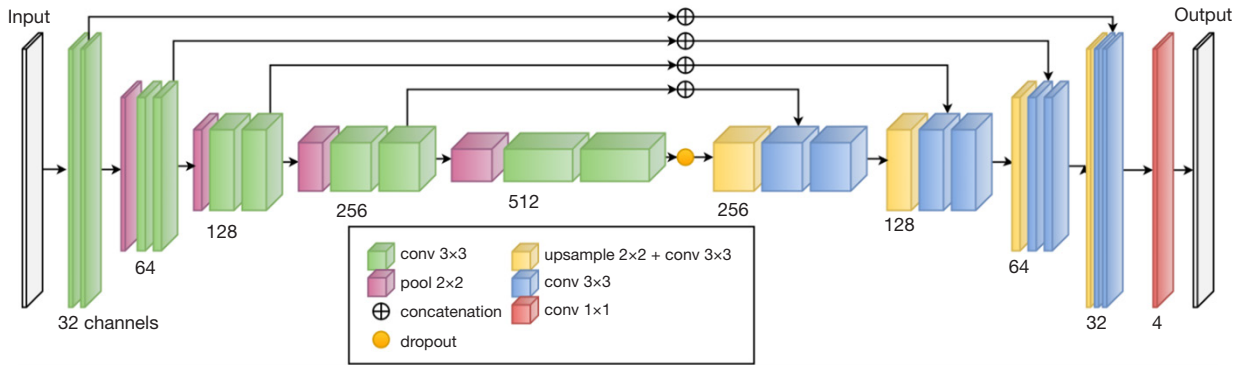

Figure 2 Diagram of the U-Net architecture used in the study.

model, we applied a density-based clustering method on the corresponding ROI to 4D DSC MRI data to refine the tumor segmentation by extracting significant data and excluding outliers, like noise, motion artifacts, or partial volume effect. Density-based clustering methods operate by identifying densely connected data points according to a selected distance, resulting in a more data-driven method as opposed to the model-driven U-Net approach. Furthermore, density-based methods are largely deterministic depending on data, *minPts*, ϵ, and distance function, in contrast to other methods such as k-means where different initialization commonly results in different outputs (34). ϵ refers to the size of the neighborhood for each data point; each data point in a cluster exists within the ϵ-neighborhood of its neighbors. *minPts* refers to the minimum number of points required for a prospective cluster to be considered a dense region. Traditional density-based spatial clustering of applications with noise (DBSCAN) algorithm is too dependent on parameters ϵ and *minPts* for reliable use across MRI scans without having standardization protocols, much less across clinical settings (34). To address this, we used a variation of DBSCAN called HDBScan as a self-adjusting algorithm that uses a range of ϵ distances for varying cluster densities (35).

According to HDBScan, the algorithm first computed the mutual reachability distance between each pair of data points, defined as the maximum between the core distances of each point and the distance between the points. The core distance is defined as the distance of the data point to its *minPts* nearest neighbor. With these mutual reachability distances, we constructed a graph representation of the data and a minimum spanning tree (MST). Sorting the edges by mutual reachability distance subsequently turns the MST into a hierarchical tree structure (dendrogram) with the largest ϵ value corresponding to the root and the smaller ϵ values corresponding to the leaf nodes. Next, the dendrogram is pruned to remove outliers. Starting from the root, each successive cluster split is retained only if both child clusters maintain a minimum of *minPts* points. If only one child cluster meets this criterion, the parent cluster keeps the points while pruning outliers within the child cluster that don't satisfy the *minPts* condition, removing them from the dendrogram.

Given the pruned dendrogram, choosing an epsilon value would result in outputting the clusters present at the corresponding mutual reachability distance level. This doesn't achieve clusters of varying densities; we need a metric to select clusters present at different levels of the dendrogram. To do so, as part of the EOM method, we selected clusters in a manner that maximizes stability, defined by Campello *et al.* (9) to be

$$S(C_i) = \sum_{x_j \in C_i} \left(\lambda_{\max}(x_j, C_i) - \lambda_{\min}(C_i) \right) = \sum_{x_j \in C_i} \frac{1}{\varepsilon_{\min}(x_j, C_i)} - \frac{1}{\varepsilon_{\max}(C_i)} \quad [1]$$

where λ is set to $\frac{1}{\epsilon}$. This equation inherently prioritizes clusters that exhibit greater persistence across a broader spectrum of ϵ values as they are ostensibly stable. The algorithm then traversed the dendrogram from the leaf nodes upwards. It assessed the stability at each node with the objective of maximizing the cumulative sum of cluster stabilities. This process culminated in the selection of clusters that correspond optimally to significant data points within the 4D DSC MRI volume. Simultaneously, it efficiently pruned extraneous noise or less significant data points in accordance with the principles of the HDBScan algorithm.

Contour complexity

To compare the precision and localized predictions between the reference standard and the refined segmentation mask output by our algorithm, we compared the boundary complexities from each resultant mask. Boundary complexity can be roughly quantified using the surface area-to-volume ratio, where a higher ratio indicates a more intricate boundary structure. However, surface area-to-volume ratios increase as the effective radius becomes smaller for the same shape. Therefore, we used the effective radius of the contours, calculated by approximating the contour as a nonuniform sphere and deriving from the volume of the contour, to attenuate this intrinsic decrease in surface area to volume ratios. The effective radius is calculated as:

$$R = \sqrt[3]{\frac{3V}{4\pi}} \quad [2]$$

This can be quickly derived from the equation for the volume of a sphere. We defined the increase in contour complexity (ICC) as the ratio of the surface area to volume ratios of the two segmented masks weighted by the effective radii of the segmented masks as follows:

$$ICC = \left(\frac{\frac{SA_2}{V_2}}{\frac{SA_1}{V_1}} \cdot \frac{R_2}{R_1} \right) - 1 \quad [3]$$

SA_1 and V_1 refer to the surface area and volume of the initial segmentation mask output by U-Net, respectively, while SA_2 and V_2 refer to the same for the refined segmentation mask output by the algorithm. R_2 and R_1 refer to the effective radius of the initial segmentation mask and the refined segmentation mask, respectively.

Performance evaluation and Pearson correlation analysis

To compare with current standard segmentation methodologies, we used the automated reference standard supplemented by manual revisions as provided by the UPENN-GBM dataset. While this reference standard is constrained by its reliance solely on 3D structural data and is susceptible to intra- and inter-observer variability, it does reflect the prevailing clinical practice for segmentation rooted in structural MRI. We also used nnU-Net and standard 2D U-Net models trained using the reference standard as ground truth for quantitative comparison to our proposed approach (36). Quantitative assessment was conducted using the Jaccard Index, or Intersection over Union (IoU), defined as the intersection of two regions divided by their union, and precision, defined as the ratio of true positives to the sum of the true positives plus false positives. We used these metrics to characterize the overlap between the proposed segmentation and the reference standard masks.

To assess the clinical relevance and possible improvement of the proposed segmentation method, we also examined the relationship between the tumor volume from the segmented tumor regions and the selected clinical outcome measurements available in the UPENN-GBM dataset. Using 54 cases that have both MRI data and documented information on KPS and post-surgery survival days, we performed a bivariate Pearson correlation analysis using the software IBM Statistical Product and Service Solutions (SPSS) Statistics 26.0 (RRID:SCR_016479) between segmented tumor volumes obtained from either our approach or the reference standard provided by the UPENN-GBM dataset with KPS and post-surgery survival days. Statistically significant relationships between these clinical data and segmented tumor volumes can be found from the Pearson correlation coefficient (r) defined as follows:

$$r_{x,y} = \frac{\mathrm{cov}_{x,y}}{\sigma_x \sigma_y} \quad [4]$$

where $\mathrm{cov}_{x,y}$ is the sample covariance of x and y, and σ_x, σ_y are the sample standard deviations (SDs) of x and y. A two-tailed significance level of $P<0.05$ was applied. Correlation between KPS and duration of survival after surgery was performed as a control to validate that the correlation analysis would detect a significant correlation between the two conditions.

Results

The reported approach by incorporating signal changes derived from the DSC-MRI time course data yielded not only tumor region segmentation akin to conventional methods but also accentuated tumor tissue by providing voxel-level hemodynamic information and distinctions, as the example shows in *Figure 3*. Notably, the tumor regions segmented using the reported approach for including time-dependent hemodynamic data from DSC perfusion MRI are different from those obtained using the standard 2D U-Net method without including the hemodynamic

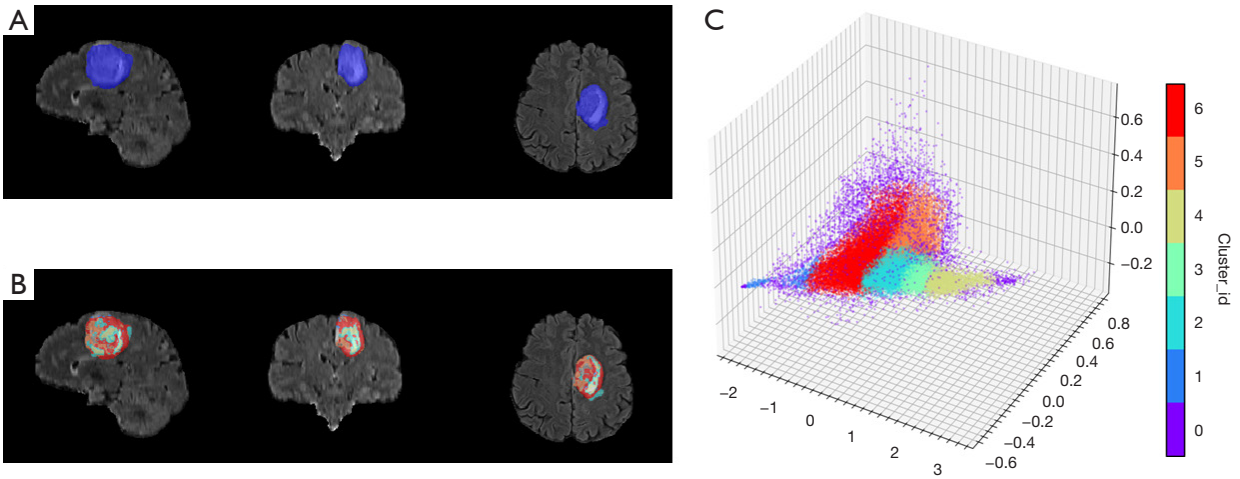

Figure 3 An example of a U-Net segmented tumor region on the axial slice using a case of diagnosed IDH1-wildtype GBM (female, 64-year-old). The tumor is in the left frontal lobe with an indistinct mass effect. Tumor region before refinement (A) after refinement with HDBScan (B), and (C) 3D projection of time courses corresponding to voxels where purple points represent outlier voxels present in tumor region (A) but not (B). IDH1, isocitrate-dehydrogenase 1 gene; GBM, glioblastoma; HDBScan, Hierarchical Density-Based Scan; 3D, three-dimensional.

Table 1 Quantitative comparison of tumor segmentation with different methods

Algorithm	IoU	Precision	Percent retention
U-Net	0.8316	0.9263	–
nnU-Net	0.87004	0.9276	–
U-Net + HDBScan (proposed)	0.7483	0.9457	0.6793±0.1398

Reference standard is the structural image-based segmentation provided by UPENN-GBM dataset. IoU and precision are presented as mean, while percent retention is presented as mean ± standard deviation. IoU, Intersection over Union; HDBScan, Hierarchical Density Based Scan; UPENN-GBM, University of Pennsylvania glioblastoma database.

information (*Figure 3A*,*3B*). This is not surprising but anticipated as segmentation relying solely on traditional T_1, T_2-weighted, and FLAIR images is predominantly based on morphological features, which provides the spatial framework for the reported methods. Importantly, intratumoral heterogeneity, which is a hallmark of GBM and many other aggressive solid tumors, is delineated in the segmented tumors (*Figure 3C*).

U-Net and density-based analysis

Compared with the 2D U-Net backbone, we retained an average of 67.93% of the voxels within the ROIs with a SD of 13.98% across the cohort of 513 subjects in total using our current density-based approach (*Table 1*). This suggests that compared to just using the U-Net architecture, which relies on 3D spatial information and contrast seen in FLAIR images, the reported approach, which utilizes 4D spatiotemporal information present in DSC MRI imaging, enhances the segmentation by reducing the size of the backbone segmentation by 32.05% on average by eliminating voxels with insignificant hemodynamic activity seen in perfusion MRI data. According to the automated reference standard provided by the UPENN-GBM dataset, the final segmentation output by our approach reached a 74.83% IoU score on average compared to 83.16% IoU score using the U-Net approach alone and 87.004% IoU using nnU-Net with 5-fold cross-validation (*Table 1*). We improved the precision from 92.63% with U-Net alone and 92.76% with nnU-Net to 94.57% using our reported approach, indicating an overall enhancement of precision in segmentation when combining 3D structural MRI data with additional hemodynamic information of the tumor from 4D DSC perfusion MRI.

Interestingly, and perhaps significantly, the obtained IoU is lower than the IoUs resulting from both the initial U-Net segmentation and the nnU-Net segmentation, signifying that perfusion MRI discerns information that is either absent or, at the very least, unique from what is acquired through 3D structural MRI. This observation is significant as prevailing tumor segmentation methods, which underpin

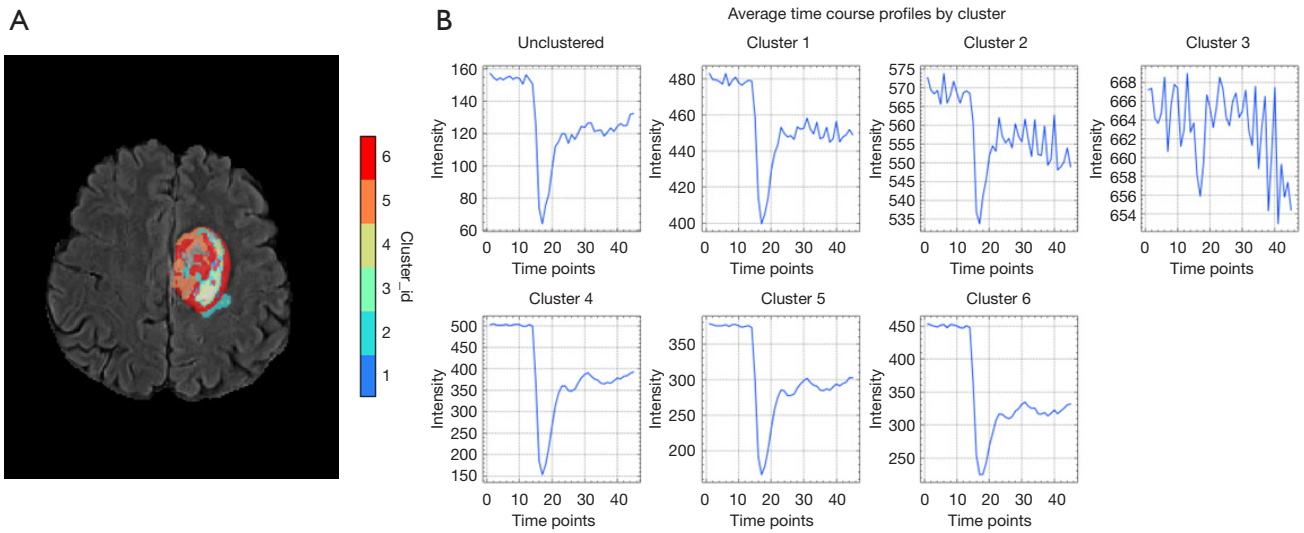

Figure 4 An example of the intratumoral heterogeneity revealed by the segmentation approach based on a IDH1-wildtype GBM tumors in a 64-year-old patient (female), also referenced in *Figure 3*. (A) Results of segmentation with tumor tissue subtypes highlighted by the cluster ID on the FLAIR image. (B) Average time course profiles of each cluster highlighted in (A) matched by cluster ID corresponding to tumor tissue subtypes found after analyzing hemodynamics in DSC MRI data. Notably, cluster 3 represents a cluster that would be classified as insignificant/inconclusive. IDH1, isocitrate-dehydrogenase 1 gene; GBM, glioblastoma; FLAIR, fluid-attenuated inversion recovery; DSC, dynamic susceptibility contrast; MRI, magnetic resonance imaging.

the reference standard, lack hemodynamic analysis. This information could be instrumental in further refining the existing reference standard for segmentations reliant on structural images or vice versa.

A notable feature of tumors segmented with additional hemodynamic information from DSC perfusion MRI is better delineation of intratumoral heterogeneity, as shown in *Figure 4*. In addition to the morphological heterogeneity highlighted by FLAIR images, the new segmentation approach revealed intratumoral physiological or hemodynamic heterogeneity based on the differences in blood perfusion and supplies to tumor tissues. The number of subregions can be highlighted based on the differences between the time course profiles of the DSC MRI data collected in tumors, which are unique for individual cases. Consistent with previous studies (23-26), our findings support the notion that blood supply to the tumor is diversely different and dependent on the type of tumor tissues and regions, evidenced by the multiple subregions identified by our algorithm. Each subregion corresponds to a separate and dense cluster within the time course data of perfusion MRI, signifying discernable patterns of blood perfusion or hemodynamic differences within the tumor.

Contour complexity

Using our current segmentation approach, the generated masks featured intricate, non-linear boundaries rather than smoother, convex hull-like boundaries using the reference standard, as exemplified in *Figure 5*. When measuring the contour complexity of the final segmentation masks as defined in our methods, we find that the final segmentation had an average of 146.92% ICC when compared to the reference standard, indicating a quantifiable increase in the complexity of the segmentation boundaries. While greater contour complexity does not inherently equate to higher accuracy in tumor segmentation, it does indicate a more refined level of tumor segmentation based on the added hemodynamic information included in our proposed method. In *Figure 5A*, *5B*, and *5E*, the tumor mask exhibits a relatively smooth, convex hull-like structure in the reference standard derived from 3D structural MRI. Our proposed approach, on the other hand, can exclude tissues within the convex region and yields more precise and localized predictions by leveraging hemodynamic information from 4D DSC MRI. This refinement, particularly evident within central regions of the tumors, leads to increased segmentation boundary complexity compared to the reference standard.

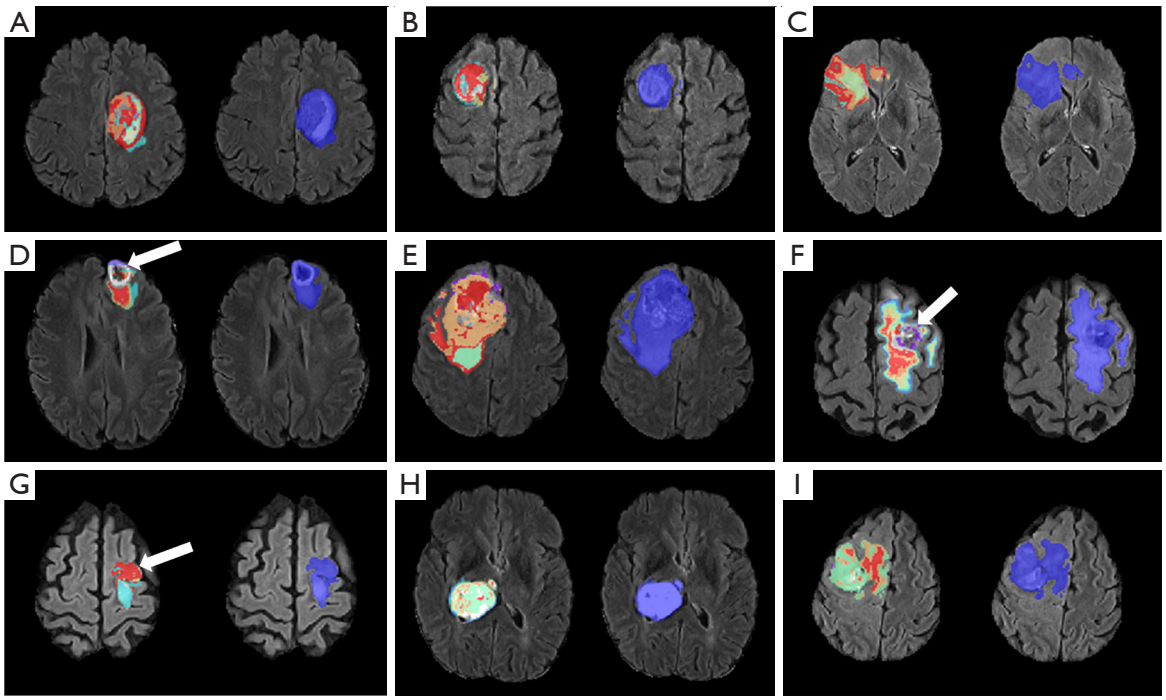

Figure 5 Selected axial slices from nine different patients with final tumor segmentation mask and reference standard segmentation mask overlaid on FLAIR images. Note case (D) and (F), where the reported algorithm excludes the necrotic core (arrows indicated), and case (G), where the algorithm focuses on the enhancing tumor region (arrow indicated). (A,D,F,G-I) are IDH1-wildtype GBM. (B,C,E) and IDH1-NOS/NEC GBM. FLAIR, fluid-attenuated inversion recovery; IDH1, isocitrate-dehydrogenase 1 gene; GBM, glioblastoma; NOS, not otherwise specified; NEC, not elsewhere classified.

Table 2 Results of pairwise bivariate correlation analysis

Selected volume	KPS		Survival (days)	
	r	P	*r*	P
Tumor volume (proposed)	−0.309	0.023	−0.128	0.358
Tumor volume (reference standard)	−0.230	0.095	−0.51	0.715

Bivariate correlation analysis performed between the KPS or days of survival after surgery with tumor volumes segmented with each method respectively. KPS, Karnofsky Performance Scale; *r*, Pearson Correlation Coefficient; P, significance (2-tailed) using 0.05 threshold for statistical significance.

In our case, the reference standard masks that act as the "ground truth" exhibited a preference for contiguous ROIs. Consequently, the supervised learning models, including nnU-Net, U-Net, and other clinically accepted 3D structural-based segmentation networks, may inadvertently encompass insignificant data points within the ROI due to inherent neural network bias aligned with the characteristics of the ground truth they are trained on, whereas our proposed algorithm, density-based, data-driven, and utilizing hemodynamics from 4D perfusion data, avoided this bias. Notably, it was challenging for our approach to segment necrotic core portions, as shown in *Figure 5D,5F*, which could be due to the absence of functional blood vessels within the necrotic core of GBM and, thus, no signal response collected from perfusion MRI. The algorithm also appeared to emphasize enhancing tumor regions (*Figure 5G*), indicating a corresponding hemodynamic response in 4D DSC perfusion data that may not be easily identified in 3D FLAIR data.

Pearson correlation analysis

In our Pearson correlation analysis with 54 subjects included in the current study, we found a significant correlation between KPS and the total tumor volume measured by our segmentation method (r=−0.309, P=0.023), while no significance was observed in comparison with the reference standard (*Table 2*, *Figure 6A*). The observed

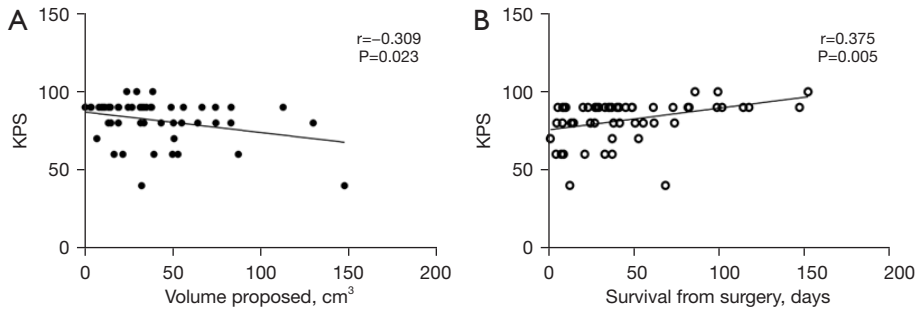

Figure 6 Graphical representation of significant results from correlation analysis on 54 subjects with line of best fit and corresponding Pearson correlation (*r*) and significance (P). (A) Correlation between KPS and tumor volume produced by proposed method. (B) Correlation between KPS and days of survival from surgery (control). KPS, Karnofsky Performance Scale.

negative correlation suggests that patients with larger tumors suffered a more pronounced functional decline. Neither segmented tumor volumes showed statistically significant correlations with the reported survival days after tumor resection surgery. When we examined the bivariate correlation between KPS and survival days after surgery, which was performed as a control for testing the sensitivity of the correlation analysis with KPS, we observed a significant correlation between these two clinical outcome measurements (r=0.375, P=0.005), indicating high relevancy and reliability of KPS for evaluating the outcome of GBM (*Figure 6B*).

Discussion

We demonstrated that using the temporal contrast changes in 4D DSC MRI data adds tumor tissue hemodynamic responses into the tumor segmentation. Conventional tumor segmentation approaches and most new deep learning-based methods typically use spatial and morphological information of structural MRI with different contrast, leaving out DSC MRI that has been routinely included in the clinical brain tumor imaging protocol. GBM typically presents high intra-tumoral heterogeneity, which is further complicated after the resection or chemo- or radiation treatment (25,26). Sole reliance on structural MRI, such as T_1-weighted, T_2-weighted, and FLAIR images, may result in overestimation and inaccurate evaluation of tumor growth and infiltration, given the presence of various forms of brain edema, including cytotoxic, vasogenic, and interstitial edema (11,12). The increased contour complexity using our proposed approach suggests that the inclusion of tissue physiological information from perfusion MRI effectively segregates or excludes voxels lacking hemodynamically active tissue. Furthermore, our algorithm excels at eliminating extraneous data points within the segmentation boundary, resulting in intricate segmentation masks characterized by greater precision and localized predictions, a departure from the smoother, more contiguous segmentation masks produced by prior methods. These extraneous data points may stem from factors such as excised tumor regions, visual artifacts during data acquisition, and other sources of noise impacting image quality. While DSC MRI data does not have high enough resolution to structurally identify most of these abnormal traits, the increased permeability disrupts the blood-brain barrier, resulting in extravasation of contrast agents, which is quantitatively measurable with DSC MRI data (17). The hemodynamic information provided by DSC MRI is especially useful in distinguishing radiation necrosis *vs.* tumor recurrence and progression (24,37). Therefore, the reported hemodynamics-incorporated segmentation approach potentially provides accurate differentiation of viable tumor tissues from other tissue types for quantitative measurements of tumor size/volume for monitoring tumor progression and treatment responses.

Our algorithm uses a 2D U-Net implementation instead of a 3D U-Net for initial structural segmentation on 3D data. Valid concerns include performance degradation and inconsistent segmentation across adjacent slices, whereas 3D U-Net would output a well-formed mask across slices. However, variable slice thickness across clinical applications in MRI makes a 2D U-Net preferable, as 2D U-Net can accommodate variable slice thickness if the 2D slice resolutions are consistent. Additionally, as spatial resolution increases with recent advances pushing sub-millimeter resolution, training a 2D U-Net is much more efficient when compared to training a 3D U-Net. Given the need for

applicability in various clinical settings, the practical benefits of a 2D U-Net implementation, particularly in addressing variable slice thickness, are still viable and adequate.

The current proof-of-concept study needs further optimization. In our study, initial segmentation is conducted using a U-Net implementation based on the information available in 3D structural images. While the addition of hemodynamic information from 4D perfusion MRI data enabled the identification of physiologically active tumor tissues and intratumor hemodynamic heterogeneity, these regions are situated within the ROIs delineated by the 3D structural data using conventional intensity-only based segmentation. As such, there exists a compelling need to optimize the backbone segmentation process to provide more dependable ROIs for the incorporation of 4D DSC perfusion MRI data. Optimizations should consider the challenges associated with working with dynamic image datasets, which are more susceptible to variations in data quality and artifacts. Given increased computational demands in dealing with complex 4D data, a simple approach is to expand U-Net's initial ROI boundaries perpendicularly. However, further research is necessary to validate the effectiveness of artificially increasing boundaries solely based on spatial considerations and determine the optimal method for expanding the boundary while preserving tumor segmentation integrity.

Worth noting is that we opted to use unsupervised learning techniques over well-established supervised learning techniques due to consideration of the inherent constraints of supervised techniques, which heavily rely on the prior ground truth annotations. Our focus is on harnessing blood perfusion information from DSC MRI data to improve tumor segmentation. Through the utilization of unsupervised techniques, which operate independently of using a reference standard as a guiding truth, we can analyze hemodynamic information to surpass the limitations of the reference standard provided by UPENN-GBM, which are rooted in 3D structural MRI imaging. Using 3D structural MRI as a foundational basis is a pattern consistent with annotations of other publicly available datasets, such as those provided as part of the Brain Tumor Segmentation Challenge (BraTS), which is the leading benchmark for evaluation and comparison of new brain segmentation techniques.

The current study used GBM perfusion MRI cases from the open-source data from the Cancer Imaging Archive. Thus, the retrospectively collected clinical data naturally are diverse. Reference standard segmentation methods used by the UPENN-GBM database were based on 3D structural images with manual revisions. They are generally well annotated but prone to intra- and inter-observer variability (27). Our algorithm is designed to refine tumor segmentation masks from existing methods and clarify uncertainties such as tissue boundaries or mitigating difficulties arising from visual assessment. While our proposed algorithm correlates well with clinical data, such as KPS scores, compared to the reference standard, robust validation against a "ground truth" is necessary to reinforce the significance of the advantages brought by the incorporation of perfusion data before warranting adoption in clinical settings. Density-based clustering can identify outliers throughout the tumor region output by the backbone structural segmentation network, not just at the boundaries, making reconciliation with asynchronous expert review difficult as manual expert review likely favors single convex bounded volumes over complex volumes with high granularity.

Intratumoral heterogeneity is a feature of solid tumors that can be considered as tissue level variations of tumor structural and biological properties. Intratumoral heterogeneity may reflect tissues or cells with distinct genotypes and phenotypes that exhibit divergent biological behaviors and functions and, therefore, need to be diagnosed and characterized for targeted or precision treatment. From a cancer imaging point of view and normally in radiology clinical practice, intratumoral heterogeneity is typically reported by observations of tissue-type specific or related different imaging contrast, for example, features shown in FLAIR images. However, those contrast differences or heterogeneity are based on structural imaging that only can show the steady state morphological differences of tumor tissue. On the other hand, all morphological differences should have their physiological bases or correlates, e.g., differences in blood supply as reported by DSC MRI. We, as well as others, have proposed and shown the hemodynamic heterogeneity of brain tumors (38-40) in previous studies. The dynamic and complex information from DSC MRI is difficult to incorporate into tumor segmentation. However, it is more physiologically relevant to tumor biological properties. We anticipate that future studies and method development will lead to tools and solutions for comprehensive imaging characterizations of tumor heterogeneity morphologically and physiologically.

The slices presented in the figures were chosen to showcase the segmentation output of our proposed

algorithm and highlight drawbacks identified during our analysis. For a more comprehensive assessment, processed data from patients not featured in the manuscript can be provided upon request from the corresponding authors.

Conclusions

By harnessing the hemodynamic information from DSC perfusion MRI data, the newly reported segmentation approach can effectively detect and identify voxels that contain physiologically distinct tumor tissue, which are not distinguishable by conventional segmentation methods that only use structural or morphological images. This new capability enables tissue physiology-informed tumor segmentation, thus enhancing the segmentation accuracy when combined with morphologic feature-based segmentation. Our findings indicate that exploring the tumor hemodynamic characteristics may provide quantitative MRI measurements that are more sensitive to tumor progression and treatment response, evidenced by outperforming the reference standard when correlated with clinical measurements of patient physiological and functional conditions. This approach has the potential to change clinical practices on brain tumor imaging, and furthermore, can be applied to other clinical indications that use perfusion MRI to assess hemodynamic properties of the tissue, such as stroke.

Acknowledgments

Funding: This work was supported in part by a grant from the National Institutes of Health (No. R01CA169937 to H.M.).

Footnote

Conflicts of Interest: All authors have completed the ICMJE uniform disclosure form (available at https://qims.amegroups.com/article/view/10.21037/qims-23-1471/coif). H.M. reports that this study was supported in part by the National Institutes of Health (No. R01CA169937). The other authors have no conflicts of interest to declare.

Ethical Statement: The authors are accountable for all aspects of the work in ensuring that questions related to the accuracy or integrity of any part of the work are appropriately investigated and resolved. The study was conducted in accordance with the Declaration of Helsinki (as revised in 2013). Because of retrospective use of these open source and de-identified data from the UPENN-GBM dataset, obtaining written informed consent from subjects was done at the original study site and not required for this study.

References

1. Wadhwa A, Bhardwaj A, Singh Verma V. A review on brain tumor segmentation of MRI images. Magn Reson Imaging 2019;61:247-59.
2. Fawzi A, Achuthan A, Belaton B. Brain Image Segmentation in Recent Years: A Narrative Review. Brain Sci 2021;11:1055.
3. Shaukat Z, Farooq QUA, Tu S, Xiao C, Ali S. A state-of-the-art technique to perform cloud-based semantic segmentation using deep learning 3D U-Net architecture. BMC Bioinformatics 2022;23:251.
4. Saeedi S, Rezayi S, Keshavarz H, R Niakan Kalhori S. MRI-based brain tumor detection using convolutional deep learning methods and chosen machine learning techniques. BMC Med Inform Decis Mak 2023;23:16.
5. Yamashita R, Nishio M, Do RKG, Togashi K. Convolutional neural networks: an overview and application in radiology. Insights Imaging 2018;9:611-29.
6. Ronneberger O, Fischer P, Brox T. U-Net: Convolutional Networks for Biomedical Image Segmentation. Lecture Notes in Computer Science 2015;9351:234-41.
7. Milletari F, Navab N, Ahmadi SA. V-Net: Fully Convolutional Neural Networks for Volumetric Medical Image Segmentation. 2016 Fourth International Conference on 3D Vision (3DV), Stanford, CA, USA, 2016:565-71.
8. Oktay O, Schlemper J, Folgoc LL, Lee M, Heinrich M, Misawa K, Mori K, McDonagh S, Hammerla NY, Kainz B, Glocker B, Rueckert D. Attention U-Net: Learning Where to Look for the Pancreas. arXiv:1804.03999.
9. Campello RJGB, Moulavi D, Sander J. Density-Based

Clustering Based on Hierarchical Density Estimates. Pacific-Asia conference on knowledge discovery and data mining. Lecture Notes in Computer Science 2013;7819:160-72.
10. Mohammed YMA, El Garouani S, Jellouli I. A survey of methods for brain tumor segmentation-based MRI images. J Comput Des Eng 2023;10:266-93.
11. Eloyan A, Yue MS, Khachatryan D. Tumor heterogeneity estimation for radiomics in cancer. Stat Med 2020;39:4704-23.
12. Fan M, Chen H, You C, Liu L, Gu Y, Peng W, Gao X, Li L. Radiomics of Tumor Heterogeneity in Longitudinal Dynamic Contrast-Enhanced Magnetic Resonance Imaging for Predicting Response to Neoadjuvant Chemotherapy in Breast Cancer. Front Mol Biosci 2021;8:622219.
13. Moradmand H, Aghamiri SMR, Ghaderi R. Impact of image preprocessing methods on reproducibility of radiomic features in multimodal magnetic resonance imaging in glioblastoma. J Appl Clin Med Phys 2020;21:179-90.
14. Boxerman JL, Quarles CC, Hu LS, Erickson BJ, Gerstner ER, Smits M, et al. Consensus recommendations for a dynamic susceptibility contrast MRI protocol for use in high-grade gliomas. Neuro Oncol 2020;22:1262-75.
15. Schmainda KM, Prah MA, Rand SD, Liu Y, Logan B, Muzi M, et al. Multisite Concordance of DSC-MRI Analysis for Brain Tumors: Results of a National Cancer Institute Quantitative Imaging Network Collaborative Project. AJNR Am J Neuroradiol 2018;39:1008-16.
16. Zhou Z, Lu ZR. Gadolinium-based contrast agents for magnetic resonance cancer imaging. Wiley Interdiscip Rev Nanomed Nanobiotechnol 2013;5:1-18.
17. Henriksen OM, Del Mar Álvarez-Torres M, Figueiredo P, Hangel G, Keil VC, Nechifor RE, Riemer F, Schmainda KM, Warnert EAH, Wiegers EC, Booth TC. High-Grade Glioma Treatment Response Monitoring Biomarkers: A Position Statement on the Evidence Supporting the Use of Advanced MRI Techniques in the Clinic, and the Latest Bench-to-Bedside Developments. Part 1: Perfusion and Diffusion Techniques. Front Oncol 2022;12:810263.
18. van Dijken BRJ, van Laar PJ, Smits M, Dankbaar JW, Enting RH, van der Hoorn A. Perfusion MRI in treatment evaluation of glioblastomas: Clinical relevance of current and future techniques. J Magn Reson Imaging 2019;49:11-22.
19. Schmainda KM, Zhang Z, Prah M, Snyder BS, Gilbert MR, Sorensen AG, Barboriak DP, Boxerman JL. Dynamic susceptibility contrast MRI measures of relative cerebral blood volume as a prognostic marker for overall survival in recurrent glioblastoma: results from the ACRIN 6677/RTOG 0625 multicenter trial. Neuro Oncol 2015;17:1148-56.
20. Hakyemez B, Erdogan C, Ercan I, Ergin N, Uysal S, Atahan S. High-grade and low-grade gliomas: differentiation by using perfusion MR imaging. Clin Radiol 2005;60:493-502.
21. Aydin S, Fatihoglu E, Kosar PN, Ergun E. Perfusion and permeability MRI in glioma grading. Egypt J Radiol Nucl Med 2020;51:2.
22. Cribaro GP, Saavedra-López E, Romarate L, Mitxitorena I, Díaz LR, Casanova PV, Roig-Martínez M, Gallego JM, Perez-Vallés A, Barcia C. Three-dimensional vascular microenvironment landscape in human glioblastoma. Acta Neuropathol Commun 2021;9:24.
23. Maral H, Ertekin E, Tunçyürek Ö, Özsunar Y. Effects of Susceptibility Artifacts on Perfusion MRI in Patients with Primary Brain Tumor: A Comparison of Arterial Spin-Labeling versus DSC. AJNR Am J Neuroradiol 2020;41:255-61.
24. Jafari-Khouzani K, Emblem KE, Kalpathy-Cramer J, Bjørnerud A, Vangel MG, Gerstner ER, Schmainda KM, Paynabar K, Wu O, Wen PY, Batchelor T, Rosen B, Stufflebeam SM. Repeatability of Cerebral Perfusion Using Dynamic Susceptibility Contrast MRI in Glioblastoma Patients. Transl Oncol 2015;8:137-46.
25. Broka A, Hysenaj Z, Sharma S, Rehmani R. Lion in Sheep's Clothing: Glioblastoma Mimicking Intracranial Hemorrhage. Cureus 2021;13:e14212.
26. Liao W, Liu Y, Wang X, Jiang X, Tang B, Fang J, Chen C, Hu Z. Differentiation of primary central nervous system lymphoma and high-grade glioma with dynamic susceptibility contrast-enhanced perfusion magnetic resonance imaging. Acta Radiol 2009;50:217-25.
27. Bakas S, Sako C, Akbari H, Bilello M, Sotiras A, Shukla G, et al. The University of Pennsylvania glioblastoma (UPenn-GBM) cohort: advanced MRI, clinical, genomics, & radiomics. Sci Data 2022;9:453.
28. Bakas S, Sako C, Akbari H, Bilello M, Sotiras A, Shukla G, et al. Multi-parametric magnetic resonance imaging (mpMRI) scans for de novo Glioblastoma (GBM) patients from the University of Pennsylvania Health System (UPENN-GBM). The Cancer Imaging Archive (TCIA) Public Access 2021. Available online: https://wiki.cancerimagingarchive.net/pages/viewpage.action?pageId=70225642

29. Clark K, Vendt B, Smith K, Freymann J, Kirby J, Koppel P, Moore S, Phillips S, Maffitt D, Pringle M, Tarbox L, Prior F. The Cancer Imaging Archive (TCIA): maintaining and operating a public information repository. J Digit Imaging 2013;26:1045-57.
30. Rohlfing T, Zahr NM, Sullivan EV, Pfefferbaum A. The SRI24 multichannel atlas of normal adult human brain structure. Hum Brain Mapp 2010;31:798-819.
31. Pedregosa F, Varoquaux G, Gramfort A, Michel V, Thirion B, Grisel O, Blondel M, Prettenhofer P, Weiss R, Dubourg V, Vanderplas J, Passos A, Cournapeau D, Brucher M, Perrot M, Duchesnay E. Scikit-learn: Machine Learning in Python. J Mach Learn Res 2011;12:2825-30.
32. McInnes L, Healy J, Astels S. hdbscan: Hierarchical density based clustering. J Open Source Softw 2017;2:205.
33. Kingma DP, Ba J. Adam: A Method for Stochastic Optimization. arXiv:1412.6980.
34. Ester M, Kriegel HP, Sander J, Xu X. A density-based algorithm for discovering clusters in large spatial databases with noise. Proceedings of the Second International Conference on Knowledge Discovery and Data Mining, 1996:226-31.
35. Malzer C, Baum M. A Hybrid Approach To Hierarchical Density-based Cluster Selection. 2020 IEEE International Conference on Multisensor Fusion and Integration for Intelligent Systems (MFI), Karlsruhe, Germany, 2020:223-8.
36. Isensee F, Jaeger PF, Kohl SAA, Petersen J, Maier-Hein KH. nnU-Net: a self-configuring method for deep learning-based biomedical image segmentation. Nat Methods 2021;18:203-11.
37. Shiroishi MS, Castellazzi G, Boxerman JL, D'Amore F, Essig M, Nguyen TB, Provenzale JM, Enterline DS, Anzalone N, Dörfler A, Rovira À, Wintermark M, Law M. Principles of T2 *-weighted dynamic susceptibility contrast MRI technique in brain tumor imaging. J Magn Reson Imaging 2015;41:296-313.
38. Ji B, Wang S, Liu Z, Weinberg BD, Yang X, Liu T, Wang L, Mao H. Revealing hemodynamic heterogeneity of gliomas based on signal profile features of dynamic susceptibility contrast-enhanced MRI. Neuroimage Clin 2019;23:101864.
39. Jeong J, Wang L, Ji B, Lei Y, Ali A, Liu T, Curran WJ, Mao H, Yang X. Machine-learning based classification of glioblastoma using delta-radiomic features derived from dynamic susceptibility contrast enhanced magnetic resonance images: Introduction. Quant Imaging Med Surg 2019;9:1201-13.
40. Liu Z, Yao B, Wen J, Wang M, Ren Y, Chen Y, Hu Z, Li Y, Liang D, Liu X, Zheng H, Luo D, Zhang N. Voxel-wise mapping of DCE-MRI time-intensity-curve profiles enables visualizing and quantifying hemodynamic heterogeneity in breast lesions. Eur Radiol 2024;34:182-92.

Cite this article as: Tang L, Wu T, Hu R, Gu Q, Yang X, Mao H. Hemodynamic property incorporated brain tumor segmentation by deep learning and density-based analysis of dynamic susceptibility contrast-enhanced magnetic resonance imaging (MRI). Quant Imaging Med Surg 2024;14(4):2774-2787. doi: 10.21037/qims-23-1471

Supplementary

Table S1 Clinical data for selected studies

ID	Gender	Age_at_scan_years	Survival_from_surgery_days	IDH1	MGMT	KPS	GTR_over90percent	Time_since_baseline_preop	PsP_TP_score
UPENN-GBM-00001_11	F	52.16	Not available	Wildtype	Not available	Not available	Y	0	NA
UPENN-GBM-00002_11	F	61.3	291	Wildtype	Not available	Not available	Y	0	NA
UPENN-GBM-00003_11	M	42.82	Not available	Wildtype	Not available	Not available	Y	0	NA
UPENN-GBM-00004_11	M	33.43	Not available	Nos/nec	Not available	Not available	Y	0	NA
UPENN-GBM-00005_11	M	53.33	Not available	Wildtype	Not available	Not available	Y	0	NA
UPENN-GBM-00006_11	M	52.99	626	Wildtype	Not available	Not available	Y	0	NA
UPENN-GBM-00007_11	M	56.96	Not available	Wildtype	Not available	Not available	Y	0	NA
UPENN-GBM-00008_11	F	55.06	469	Wildtype	Not available	Not available	Y	0	NA
UPENN-GBM-00009_11	M	69.12	561	Wildtype	Not available	Not available	Y	0	NA
UPENN-GBM-00010_11	M	77.54	Not available	Wildtype	Not available	Not available	Y	0	NA
UPENN-GBM-00011_11	F	39.61	798	NOS/NEC	Not available	Not available	Y	0	NA
UPENN-GBM-00012_11	M	53.85	882	Wildtype	Not available	Not available	Y	0	NA
UPENN-GBM-00014_11	M	68.06	272	Wildtype	Not available	Not available	Y	0	NA
UPENN-GBM-00015_11	M	54.9	Not available	Wildtype	Not available	Not available	Y	0	NA
UPENN-GBM-00016_11	M	70.89	509	Wildtype	Not available	Not available	Y	0	NA
UPENN-GBM-00018_11	F	57.21	1170	Wildtype	Not available	Not available	Y	0	NA
UPENN-GBM-00019_11	F	43.12	Not available	Wildtype	Not available	Not available	Y	0	NA
UPENN-GBM-00020_11	M	50.86	425	Wildtype	Not available	Not available	Y	0	NA
UPENN-GBM-00021_11	F	49.04	510	Wildtype	Not available	Not available	Y	0	NA
UPENN-GBM-00022_11	F	53.88	1882	Wildtype	Unmethylated	Not available	Not available	0	NA
UPENN-GBM-00023_11	M	55.57	Not available	Wildtype	Not available	Not available	N	0	NA
UPENN-GBM-00024_11	M	54.26	Not available	Wildtype	Not available	Not available	Y	0	NA
UPENN-GBM-00025_11	F	64.32	Not available	Wildtype	Not available	Not available	Y	0	NA
UPENN-GBM-00027_11	F	65.08	Not available	Wildtype	Not available	Not available	Y	0	NA
UPENN-GBM-00028_11	F	67.35	Not available	Wildtype	Not available	Not available	N	0	NA
UPENN-GBM-00029_11	M	22.03	1504	Wildtype	Not available	Not available	Y	0	NA
UPENN-GBM-00030_11	M	66.81	502	Wildtype	Not available	Not available	Y	0	NA
UPENN-GBM-00031_11	M	65.92	2207	Wildtype	Not available	Not available	N	0	NA
UPENN-GBM-00032_11	M	63.26	Not available	Nos/nec	Not available	Not available	Y	0	NA
UPENN-GBM-00033_11	M	60.52	707	Wildtype	Not available	Not available	Y	0	NA
UPENN-GBM-00034_11	F	53.63	464	Wildtype	Unmethylated	Not available	N	0	NA
UPENN-GBM-00035_11	M	56.25	364	Wildtype	Not available	Not available	Y	0	NA
UPENN-GBM-00036_11	M	42.14	Not available	Wildtype	Not available	Not available	Y	0	NA
UPENN-GBM-00036_21	M	43.57	Not available	Wildtype	Not available	Not available	Not applicable	521	6
UPENN-GBM-00038_11	M	57.99	Not available	Wildtype	Not available	Not available	N	0	NA
UPENN-GBM-00039_11	F	64.5	Not available	Wildtype	Not available	Not available	Y	0	NA
UPENN-GBM-00040_11	M	52.45	360	Wildtype	Not available	Not available	Y	0	NA
UPENN-GBM-00041_11	M	65.65	598	Wildtype	Not available	Not available	Y	0	NA
UPENN-GBM-00042_11	M	62.05	Not available	Wildtype	Not available	Not available	Y	0	NA
UPENN-GBM-00042_21	M	62.83	Not available	Nos/nec	Not available	Not available	Not applicable	282	6
UPENN-GBM-00043_11	M	63.48	172	NOS/NEC	Not available	Not available	Y	0	NA
UPENN-GBM-00044_11	M	63.41	Not available	Wildtype	Not available	Not available	Y	0	NA
UPENN-GBM-00045_11	F	50.8	538	Wildtype	Not available	Not available	Y	0	NA
UPENN-GBM-00045_21	F	51.11	Not available	Nos/nec	Not available	Not available	Not applicable	113	2
UPENN-GBM-00046_11	M	58.75	Not available	Wildtype	Not available	Not available	Y	0	NA
UPENN-GBM-00047_11	M	63.44	437	NOS/NEC	Not available	Not available	Y	0	NA
UPENN-GBM-00048_11	M	65.22	Not available	Wildtype	Not available	Not available	N	0	NA
UPENN-GBM-00050_11	M	54.04	Not available	Wildtype	Not available	Not available	Y	0	NA
UPENN-GBM-00051_11	F	60.21	Not available	Wildtype	Not available	Not available	Y	0	NA
UPENN-GBM-00051_21	F	61.26	Not available	Wildtype	Not available	Not available	Not applicable	385	6
UPENN-GBM-00052_11	M	53.35	Not available	Nos/nec	Not available	Not available	Y	0	NA
UPENN-GBM-00052_21	M	54.34	Not available	Wildtype	Not available	Not available	Not applicable	362	6
UPENN-GBM-00053_11	M	64	Not available	Wildtype	Not available	Not available	Y	0	NA
UPENN-GBM-00054_11	F	39.88	412	NOS/NEC	Not available	Not available	Y	0	NA
UPENN-GBM-00055_11	M	57.87	Not available	Wildtype	Not available	Not available	Y	0	NA
UPENN-GBM-00055_21	M	57.96	Not available	Nos/nec	Not available	Not available	Not applicable	31	5
UPENN-GBM-00056_11	F	68.84	Not available	Wildtype	Not available	Not available	Y	0	NA
UPENN-GBM-00057_11	M	65.95	673	Wildtype	Not available	Not available	Y	0	NA
UPENN-GBM-00058_11	M	50.92	392	Wildtype	Not available	Not available	Y	0	NA
UPENN-GBM-00059_11	M	56.53	369	Wildtype	Not available	Not available	Y	0	NA
UPENN-GBM-00060_11	M	59.07	445	Wildtype	Not available	Not available	Y	0	NA
UPENN-GBM-00061_11	M	60.22	Not available	Nos/nec	Not available	Not available	N	0	NA
UPENN-GBM-00062_11	M	61.4	427	Wildtype	Not available	Not available	Y	0	NA
UPENN-GBM-00063_11	F	80.8	1152	Wildtype	Not available	Not available	Y	0	NA
UPENN-GBM-00064_11	F	73.75	879	Wildtype	Not available	Not available	Y	0	NA
UPENN-GBM-00065_11	F	75.64	111	NOS/NEC	Not available	Not available	Y	0	NA
UPENN-GBM-00066_11	F	62.46	493	Wildtype	Not available	Not available	Y	0	NA
UPENN-GBM-00067_11	F	72.39	Not available	Nos/nec	Not available	Not available	Y	0	NA
UPENN-GBM-00068_11	M	52.2	389	Wildtype	Indeterminate	Not available	Y	0	NA
UPENN-GBM-00069_11	M	50.77	296	Wildtype	Not available	Not available	Y	0	NA
UPENN-GBM-00070_11	F	75.63	Not available	Wildtype	Not available	Not available	Y	0	NA
UPENN-GBM-00071_11	F	37.13	Not available	Mutated	Not available	Not available	Y	0	NA
UPENN-GBM-00072_11	F	59.79	553	Wildtype	Not available	Not available	Y	0	NA
UPENN-GBM-00073_11	M	68.99	291	NOS/NEC	Not available	Not available	Y	0	NA
UPENN-GBM-00074_11	M	56.51	Not available	Nos/nec	Not available	Not available	Y	0	NA
UPENN-GBM-00075_11	M	54.1	278	Wildtype	Not available	Not available	Y	0	NA
UPENN-GBM-00076_11	M	61.42	54	NOS/NEC	Not available	Not available	Not available	0	NA
UPENN-GBM-00077_11	M	80.93	54	Wildtype	Not available	Not available	Y	0	NA
UPENN-GBM-00078_11	M	70.74	158	Wildtype	Indeterminate	Not available	Y	0	NA
UPENN-GBM-00079_11	F	78.67	Not available	Nos/nec	Not available	Not available	Y	0	NA
UPENN-GBM-00080_11	F	57.71	583	NOS/NEC	Not available	Not available	Y	0	NA
UPENN-GBM-00081_11	M	63	24	NOS/NEC	Not available	Not available	Y	0	NA
UPENN-GBM-00082_11	M	44.78	351	Wildtype	Indeterminate	Not available	Y	0	NA
UPENN-GBM-00083_11	M	68.78	333	Wildtype	Not available	60	Y	0	NA
UPENN-GBM-00084_11	F	47.22	Not available	Wildtype	Not available	Not available	Y	0	NA
UPENN-GBM-00084_21	F	47.63	Not available	Nos/nec	Not available	Not available	Not applicable	151	2
UPENN-GBM-00085_11	M	48.18	Not available	Wildtype	Not available	Not available	Y	0	NA
UPENN-GBM-00086_11	M	70.81	146	Wildtype	Not available	Not available	N	0	NA
UPENN-GBM-00086_21	M	71.13	Not available	Wildtype	Not available	Not available	Not applicable	116	4
UPENN-GBM-00087_11	M	71.76	44	NOS/NEC	Not available	Not available	Y	0	NA
UPENN-GBM-00088_11	M	47.32	334	Wildtype	Unmethylated	90	Y	0	NA
UPENN-GBM-00088_21	M	47.92	Not available	Wildtype	Indeterminate	Not available	Not applicable	221	5
UPENN-GBM-00089_11	M	77.37	1475	Wildtype	Not available	90	Y	0	NA
UPENN-GBM-00090_11	F	66.91	Not available	Wildtype	Not available	Not available	N	0	NA
UPENN-GBM-00091_11	M	70.54	200	Wildtype	Unmethylated	Not available	N	0	NA
UPENN-GBM-00092_11	F	66.44	Not available	Wildtype	Unmethylated	80	Y	0	NA
UPENN-GBM-00093_21	F	52.21	Not available	Wildtype	Unmethylated	Not available	Not applicable	332	5
UPENN-GBM-00097_11	M	57.01	Not available	Wildtype	Not available	90	N	0	NA
UPENN-GBM-00098_11	F	62.67	524	Wildtype	Methylated	Not available	Y	0	NA
UPENN-GBM-00100_11	M	46.18	205	NOS/NEC	Not available	Not available	N	0	NA
UPENN-GBM-00101_11	M	60.9	339	NOS/NEC	Not available	Not available	N	0	NA
UPENN-GBM-00102_11	M	77.43	106	NOS/NEC	Not available	Not available	Y	0	NA
UPENN-GBM-00103_11	F	78.68	Not available	Nos/nec	Not available	Not available	N	0	NA
UPENN-GBM-00104_11	F	73.09	Not available	Wildtype	Not available	Not available	N	0	NA
UPENN-GBM-00105_11	F	74.05	32	NOS/NEC	Not available	Not available	N	0	NA
UPENN-GBM-00106_11	F	72.4	104	NOS/NEC	Not available	Not available	Y	0	NA
UPENN-GBM-00107_11	M	54.35	472	NOS/NEC	Not available	Not available	N	0	NA
UPENN-GBM-00108_11	M	66.99	173	NOS/NEC	Not available	Not available	N	0	NA
UPENN-GBM-00109_11	M	51.02	Not available	Nos/nec	Not available	Not available	Y	0	NA
UPENN-GBM-00110_11	F	61.44	Not available	Nos/nec	Not available	Not available	N	0	NA
UPENN-GBM-00111_11	M	72.49	Not available	Nos/nec	Not available	Not available	N	0	NA
UPENN-GBM-00112_11	M	64.07	494	NOS/NEC	Not available	Not available	Y	0	NA
UPENN-GBM-00113_11	F	68.8	479	Wildtype	Not available	Not available	Y	0	NA
UPENN-GBM-00114_11	F	47.1	1302	NOS/NEC	Not available	Not available	Y	0	NA
UPENN-GBM-00115_11	F	72.36	87	Wildtype	Methylated	Not available	N	0	NA
UPENN-GBM-00116_11	M	56.56	Not available	Wildtype	Not available	90	N	0	NA
UPENN-GBM-00119_11	F	54.1	84	Wildtype	Indeterminate	80	Y	0	NA
UPENN-GBM-00120_11	F	78.75	Not available	Wildtype	Unmethylated	90	N	0	NA
UPENN-GBM-00121_11	M	58.52	226	Wildtype	Unmethylated	Not available	N	0	NA
UPENN-GBM-00122_11	M	64.22	284	Wildtype	Unmethylated	90	Y	0	NA
UPENN-GBM-00122_21	M	64.85	Not available	Wildtype	Unmethylated	Not available	Not applicable	229	4
UPENN-GBM-00123_11	F	24.61	Not available	Mutated	Not available	Not available	Not available	0	NA
UPENN-GBM-00125_11	F	23.96	1525	Wildtype	Unmethylated	100	Y	0	NA
UPENN-GBM-00126_11	M	50.76	766	Wildtype	Indeterminate	Not available	N	0	NA
UPENN-GBM-00127_11	M	68.85	721	Wildtype	Not available	Not available	Y	0	NA
UPENN-GBM-00128_11	F	81.29	990	Wildtype	Methylated	90	Y	0	NA
UPENN-GBM-00128_21	F	81.54	Not available	Wildtype	Methylated	Not available	Not applicable	92	6

Table S1 *(continued)*

Table S1 *(continued)*

ID	Gender	Age_at_scan_years	Survival_from_surgery_days	IDH1	MGMT	KPS	GTR_over90percent	Time_since_baseline_preop	PsP_TP_score
UPENN-GBM-00129_11	M	57.59	171	Wildtype	Unmethylated	Not available	Y	0	NA
UPENN-GBM-00129_21	M	57.86	Not available	Nos/nec	Not available	Not available	Not applicable	98	3
UPENN-GBM-00130_21	M	53.71	Not available	Wildtype	Methylated	Not available	Not applicable	444	5
UPENN-GBM-00131_11	M	76.3	852	Wildtype	Methylated	Not available	Y	0	NA
UPENN-GBM-00132_11	M	48.02	922	Wildtype	Unmethylated	Not available	Y	0	NA
UPENN-GBM-00133_11	M	73.2	744	Wildtype	Unmethylated	Not available	Y	0	NA
UPENN-GBM-00133_21	M	73.72	Not available	Wildtype	Not available	Not available	Not applicable	190	5
UPENN-GBM-00134_11	M	45.03	494	Wildtype	Unmethylated	90	Y	0	NA
UPENN-GBM-00134_21	M	45.34	Not available	Wildtype	Unmethylated	Not available	Not applicable	112	5
UPENN-GBM-00135_11	M	55.59	879	Wildtype	Methylated	Not available	N	0	NA
UPENN-GBM-00137_11	M	47.47	320	Wildtype	Indeterminate	Not available	N	0	NA
UPENN-GBM-00138_11	F	60.66	1527	Wildtype	Methylated	Not available	N	0	NA
UPENN-GBM-00139_11	M	58.52	208	Wildtype	Unmethylated	Not available	N	0	NA
UPENN-GBM-00140_11	M	47.22	664	Wildtype	Unmethylated	Not available	Y	0	NA
UPENN-GBM-00140_21	M	48.37	Not available	Wildtype	Unmethylated	Not available	Not applicable	420	5
UPENN-GBM-00141_11	M	78.41	528	Wildtype	Unmethylated	Not available	N	0	NA
UPENN-GBM-00141_21	M	78.95	Not available	Wildtype	Not available	Not available	Not applicable	196	4
UPENN-GBM-00143_11	M	40.04	411	Wildtype	Unmethylated	Not available	Y	0	NA
UPENN-GBM-00144_11	F	53.07	270	Wildtype	Unmethylated	Not available	Y	0	NA
UPENN-GBM-00145_11	F	65.81	351	Wildtype	Unmethylated	Not available	Y	0	NA
UPENN-GBM-00145_21	F	66.53	Not available	Wildtype	Not available	Not available	Not applicable	263	3
UPENN-GBM-00146_11	M	48.74	1178	Wildtype	Unmethylated	90	Y	0	NA
UPENN-GBM-00148_11	M	55.51	604	Wildtype	Unmethylated	Not available	Y	0	NA
UPENN-GBM-00148_21	M	56.31	Not available	Wildtype	Unmethylated	Not available	Not applicable	295	1
UPENN-GBM-00149_11	F	69.3	233	Wildtype	Unmethylated	Not available	N	0	NA
UPENN-GBM-00150_11	F	55.95	733	Wildtype	Unmethylated	90	Y	0	NA
UPENN-GBM-00150_21	F	56.4	Not available	Wildtype	Unmethylated	Not available	Not applicable	165	5
UPENN-GBM-00151_11	M	67.43	618	Wildtype	Unmethylated	Not available	Y	0	NA
UPENN-GBM-00152_11	F	57.4	742	NOS/NEC	Not available	Not available	Y	0	NA
UPENN-GBM-00153_11	M	59.91	Not available	Nos/nec	Not available	Not available	Not available	0	NA
UPENN-GBM-00154_11	F	72.11	209	Wildtype	Not available	Not available	Y	0	NA
UPENN-GBM-00155_11	F	69.13	Not available	Nos/nec	Not available	Not available	N	0	NA
UPENN-GBM-00156_11	F	70.14	359	Wildtype	Not available	Not available	Y	0	NA
UPENN-GBM-00157_11	F	61.39	235	NOS/NEC	Not available	Not available	N	0	NA
UPENN-GBM-00158_11	M	69.68	152	NOS/NEC	Not available	Not available	Y	0	NA
UPENN-GBM-00160_11	F	58.84	Not available	Nos/nec	Not available	Not available	Y	0	NA
UPENN-GBM-00160_21	F	61	Not available	Nos/nec	Not available	Not available	Not applicable	788	6
UPENN-GBM-00161_11	F	59.81	80	NOS/NEC	Not available	Not available	Y	0	NA
UPENN-GBM-00162_11	F	73.49	557	NOS/NEC	Not available	Not available	Y	0	NA
UPENN-GBM-00163_11	F	63.78	Not available	Wildtype	Indeterminate	Not available	N	0	NA
UPENN-GBM-00164_11	F	46.79	1193	Wildtype	Not available	Not available	N	0	NA
UPENN-GBM-00165_11	M	66.64	44	Wildtype	Not available	Not available	N	0	NA
UPENN-GBM-00166_11	F	52.31	388	Wildtype	Not available	Not available	Y	0	NA
UPENN-GBM-00167_11	M	65.36	94	NOS/NEC	Not available	Not available	Y	0	NA
UPENN-GBM-00168_11	M	76.99	93	NOS/NEC	Not available	Not available	N	0	NA
UPENN-GBM-00169_11	F	72.09	23	NOS/NEC	Not available	Not available	Y	0	NA
UPENN-GBM-00170_11	M	51.79	505	Wildtype	Not available	Not available	N	0	NA
UPENN-GBM-00171_11	M	68.93	846	Wildtype	Not available	Not available	Y	0	NA
UPENN-GBM-00172_11	M	63.02	457	Wildtype	Not available	Not available	Y	0	NA
UPENN-GBM-00173_11	M	75.76	233	Wildtype	Not available	Not available	Y	0	NA
UPENN-GBM-00174_11	M	37.3	1615	NOS/NEC	Not available	Not available	Not available	0	NA
UPENN-GBM-00175_11	M	80.06	98	NOS/NEC	Not available	Not available	Y	0	NA
UPENN-GBM-00176_11	F	80.45	56	NOS/NEC	Not available	Not available	Y	0	NA
UPENN-GBM-00177_11	F	67.52	154	Wildtype	Not available	Not available	Y	0	NA
UPENN-GBM-00178_11	F	86.87	276	Wildtype	Not available	Not available	Y	0	NA
UPENN-GBM-00179_11	M	43.42	Not available	Nos/nec	Not available	Not available	Y	0	NA
UPENN-GBM-00180_11	F	60.99	146	Wildtype	Not available	Not available	Y	0	NA
UPENN-GBM-00181_11	M	54.49	Not available	Nos/nec	Not available	Not available	Y	0	NA
UPENN-GBM-00182_11	M	75.93	Not available	Nos/nec	Not available	Not available	Y	0	NA
UPENN-GBM-00183_11	F	55.87	1829	Wildtype	Not available	Not available	Y	0	NA
UPENN-GBM-00183_21	F	57.64	Not available	Wildtype	Methylated	Not available	Not applicable	648	6
UPENN-GBM-00184_11	M	85.46	Not available	Nos/nec	Not available	Not available	Y	0	NA
UPENN-GBM-00185_11	F	88.5	200	Wildtype	Not available	Not available	Y	0	NA
UPENN-GBM-00186_11	F	55.35	Not available	Wildtype	Not available	Not available	Y	0	NA
UPENN-GBM-00187_11	F	55.09	1346	Wildtype	Not available	Not available	Y	0	NA
UPENN-GBM-00188_11	M	44.46	Not available	Nos/nec	Not available	Not available	Y	0	NA
UPENN-GBM-00189_11	F	69.46	382	NOS/NEC	Not available	Not available	Y	0	NA
UPENN-GBM-00190_11	M	56.66	136	Wildtype	Not available	Not available	Y	0	NA
UPENN-GBM-00191_11	F	57.63	51	NOS/NEC	Not available	Not available	Y	0	NA
UPENN-GBM-00192_11	M	61.66	1356	NOS/NEC	Not available	Not available	Not available	0	NA
UPENN-GBM-00193_11	F	71.23	12	Wildtype	Not available	Not available	N	0	NA
UPENN-GBM-00194_11	F	59.3	250	NOS/NEC	Not available	Not available	Y	0	NA
UPENN-GBM-00195_11	M	79.51	168	NOS/NEC	Not available	Not available	Y	0	NA
UPENN-GBM-00196_11	F	86.21	21	NOS/NEC	Not available	Not available	Y	0	NA
UPENN-GBM-00197_11	M	50.03	1227	Wildtype	Methylated	Not available	Y	0	NA
UPENN-GBM-00197_21	M	52.79	Not available	Wildtype	Methylated	Not available	Not applicable	1010	6
UPENN-GBM-00198_11	M	52.61	1008	Wildtype	Not available	Not available	Y	0	NA
UPENN-GBM-00200_11	M	82.36	Not available	Nos/nec	Not available	Not available	Y	0	NA
UPENN-GBM-00201_11	M	52.84	182	Wildtype	Not available	Not available	Y	0	NA
UPENN-GBM-00202_11	M	79.27	Not available	Nos/nec	Not available	Not available	Y	0	NA
UPENN-GBM-00203_11	M	59.44	122	NOS/NEC	Not available	Not available	Y	0	NA
UPENN-GBM-00204_11	M	54.24	374	Wildtype	Not available	Not available	Y	0	NA
UPENN-GBM-00205_11	F	83.59	277	NOS/NEC	Not available	Not available	Y	0	NA
UPENN-GBM-00206_11	F	64.24	586	Wildtype	Not available	Not available	Y	0	NA
UPENN-GBM-00207_11	F	61.71	301	Wildtype	Not available	Not available	Y	0	NA
UPENN-GBM-00208_11	M	45.87	622	Wildtype	Not available	Not available	Y	0	NA
UPENN-GBM-00209_11	F	68.42	Not available	Wildtype	Not available	Not available	N	0	NA
UPENN-GBM-00210_11	M	53.95	3	Wildtype	Not available	Not available	Y	0	NA
UPENN-GBM-00212_11	M	85.74	Not available	Wildtype	Not available	Not available	Y	0	NA
UPENN-GBM-00213_11	M	76.37	73	NOS/NEC	Not available	Not available	Y	0	NA
UPENN-GBM-00214_11	M	74.52	Not available	Nos/nec	Not available	Not available	Y	0	NA
UPENN-GBM-00215_11	M	65.07	155	NOS/NEC	Not available	Not available	Y	0	NA
UPENN-GBM-00216_11	F	59.29	167	NOS/NEC	Not available	Not available	Y	0	NA
UPENN-GBM-00217_11	M	73.29	393	NOS/NEC	Not available	Not available	Y	0	NA
UPENN-GBM-00218_11	F	77.97	Not available	Wildtype	Not available	Not available	Y	0	NA
UPENN-GBM-00219_11	M	67.31	453	Wildtype	Not available	Not available	Y	0	NA
UPENN-GBM-00221_11	F	76.69	Not available	Wildtype	Not available	Not available	Y	0	NA
UPENN-GBM-00222_11	F	72.67	Not available	Nos/nec	Not available	Not available	Y	0	NA
UPENN-GBM-00223_11	F	69.33	Not available	Nos/nec	Not available	Not available	Y	0	NA
UPENN-GBM-00224_11	F	49.31	438	Wildtype	Not available	Not available	Y	0	NA
UPENN-GBM-00225_11	M	83.54	16	NOS/NEC	Not available	Not available	Y	0	NA
UPENN-GBM-00226_11	M	56.3	182	Wildtype	Not available	Not available	Y	0	NA
UPENN-GBM-00227_11	F	53.5	138	Wildtype	Not available	Not available	Y	0	NA
UPENN-GBM-00228_11	M	47.2	379	Wildtype	Not available	Not available	Y	0	NA
UPENN-GBM-00229_11	M	43.46	Not available	Mutated	Not available	Not available	Not available	0	NA
UPENN-GBM-00230_11	F	72.28	Not available	Wildtype	Not available	Not available	Y	0	NA
UPENN-GBM-00231_11	M	67.83	Not available	Wildtype	Not available	Not available	Y	0	NA
UPENN-GBM-00232_11	F	75.64	187	Wildtype	Not available	Not available	N	0	NA
UPENN-GBM-00233_11	F	63.82	Not available	Wildtype	Not available	Not available	Y	0	NA
UPENN-GBM-00234_11	M	62.82	370	Wildtype	Not available	Not available	N	0	NA
UPENN-GBM-00235_11	F	80.6	253	Wildtype	Indeterminate	Not available	N	0	NA
UPENN-GBM-00236_11	F	76.22	480	Wildtype	Not available	Not available	N	0	NA
UPENN-GBM-00237_11	M	63.62	200	Wildtype	Not available	Not available	N	0	NA
UPENN-GBM-00238_11	F	65.89	1148	Wildtype	Not available	Not available	Y	0	NA
UPENN-GBM-00239_11	F	80.89	Not available	Wildtype	Not available	Not available	N	0	NA
UPENN-GBM-00240_11	M	85.88	78	Wildtype	Methylated	Not available	Y	0	NA
UPENN-GBM-00241_11	F	71.43	Not available	Wildtype	Not available	Not available	Y	0	NA
UPENN-GBM-00242_11	F	55.7	276	Wildtype	Not available	90	N	0	NA
UPENN-GBM-00243_11	F	66.43	419	Wildtype	Not available	80	Y	0	NA
UPENN-GBM-00244_11	M	59.75	420	Wildtype	Unmethylated	Not available	N	0	NA
UPENN-GBM-00245_11	F	63.42	Not available	Wildtype	Indeterminate	Not available	Y	0	NA
UPENN-GBM-00246_11	M	75.06	51	Wildtype	Unmethylated	80	N	0	NA
UPENN-GBM-00248_11	F	45.71	Not available	Wildtype	Not available	Not available	Y	0	NA
UPENN-GBM-00249_11	F	28.2	1791	Mutated	Not available	Not available	Y	0	NA
UPENN-GBM-00250_11	F	59.79	460	Wildtype	Not available	Not available	Y	0	NA
UPENN-GBM-00251_11	F	75.67	167	Wildtype	Not available	Not available	Not available	0	NA
UPENN-GBM-00252_11	F	67.86	443	NOS/NEC	Not available	Not available	N	0	NA
UPENN-GBM-00253_11	F	86.95	349	NOS/NEC	Not available	Not available	Y	0	NA

Table S1 *(continued)*

Table S1 *(continued)*

ID	Gender	Age_at_scan_years	Survival_from_surgery_days	IDH1	MGMT	KPS	GTR_over90percent	Time_since_baseline_preop	PsP_TP_score
UPENN-GBM-00254_11	M	57.08	400	Wildtype	Not available	Not available	Not available	0	NA
UPENN-GBM-00255_11	F	64.86	80	NOS/NEC	Not available	Not available	N	0	NA
UPENN-GBM-00256_11	F	67.2	115	NOS/NEC	Not available	Not available	N	0	NA
UPENN-GBM-00258_11	M	50.71	Not available	Nos/nec	Not available	Not available	Y	0	NA
UPENN-GBM-00259_11	F	80.31	193	Wildtype	Not available	Not available	Y	0	NA
UPENN-GBM-00261_11	M	75.88	48	Wildtype	Indeterminate	Not available	Y	0	NA
UPENN-GBM-00262_11	M	70.75	580	Wildtype	Unmethylated	Not available	Y	0	NA
UPENN-GBM-00263_11	M	66.23	796	Wildtype	Methylated	Not available	Y	0	NA
UPENN-GBM-00264_11	F	61.82	1145	Wildtype	Methylated	90	N	0	NA
UPENN-GBM-00265_11	M	53.08	1062	Wildtype	Indeterminate	Not available	Y	0	NA
UPENN-GBM-00266_11	F	66.84	390	Wildtype	Not available	Not available	N	0	NA
UPENN-GBM-00267_11	F	55.13	537	Wildtype	Unmethylated	Not available	Y	0	NA
UPENN-GBM-00267_21	F	55.61	Not available	Wildtype	Unmethylated	Not available	Not applicable	176	2
UPENN-GBM-00268_11	F	82.8	20	Wildtype	Indeterminate	Not available	N	0	NA
UPENN-GBM-00269_11	M	56.21	Not available	Wildtype	Methylated	Not available	Y	0	NA
UPENN-GBM-00270_11	F	64.67	58	Wildtype	Not available	Not available	Y	0	NA
UPENN-GBM-00271_11	M	53.83	473	NOS/NEC	Not available	Not available	Y	0	NA
UPENN-GBM-00274_11	M	41.2	1021	Wildtype	Not available	Not available	Y	0	NA
UPENN-GBM-00275_11	M	46.9	454	Wildtype	Not available	Not available	Y	0	NA
UPENN-GBM-00276_11	M	18.65	Not available	Nos/nec	Not available	Not available	Y	0	NA
UPENN-GBM-00277_11	M	55.68	403	Wildtype	Not available	Not available	Y	0	NA
UPENN-GBM-00278_11	F	63.42	Not available	Wildtype	Not available	Not available	N	0	NA
UPENN-GBM-00279_11	M	68.34	Not available	Wildtype	Not available	Not available	Y	0	NA
UPENN-GBM-00280_21	M	58.41	Not available	Nos/nec	Not available	Not available	Not applicable	472	2
UPENN-GBM-00282_11	M	68.54	363	Wildtype	Unmethylated	Not available	N	0	NA
UPENN-GBM-00284_11	F	82.87	77	Wildtype	Indeterminate	60	N	0	NA
UPENN-GBM-00285_11	F	59.98	427	Wildtype	Not available	Not available	N	0	NA
UPENN-GBM-00285_21	F	60.26	Not available	Nos/nec	Not available	Not available	Not applicable	103	6
UPENN-GBM-00287_11	M	50.93	781	Mutated	Methylated	Not available	Y	0	NA
UPENN-GBM-00288_11	M	79.63	31	Wildtype	Not available	Not available	N	0	NA
UPENN-GBM-00290_11	F	82.36	409	Wildtype	Unmethylated	90	Y	0	NA
UPENN-GBM-00291_11	M	58.61	530	Wildtype	Not available	Not available	N	0	NA
UPENN-GBM-00294_11	F	60.37	112	Wildtype	Unmethylated	Not Available	N	0	NA
UPENN-GBM-00295_11	M	65.19	696	Wildtype	Indeterminate	Not Available	Y	0	NA
UPENN-GBM-00295_21	M	65.67	Not available	Wildtype	Indeterminate	Not available	Not applicable	178	5
UPENN-GBM-00296_11	M	72.15	326	Wildtype	Not available	Not available	N	0	NA
UPENN-GBM-00300_11	F	82.88	Not available	Wildtype	Not available	Not available	N	0	NA
UPENN-GBM-00301_11	M	58.18	653	Wildtype	Unmethylated	Not available	Y	0	NA
UPENN-GBM-00301_21	M	59.2	Not available	Wildtype	Not available	Not available	Not applicable	370	6
UPENN-GBM-00302_11	M	59.99	1451	Wildtype	Methylated	Not available	Y	0	NA
UPENN-GBM-00302_21	M	61.79	Not available	Wildtype	Not available	Not available	Not applicable	657	1
UPENN-GBM-00303_11	F	78.58	658	Wildtype	Not available	Not available	Y	0	NA
UPENN-GBM-00304_11	M	71.06	428	Wildtype	Unmethylated	Not available	N	0	NA
UPENN-GBM-00305_11	M	76.88	92	NOS/NEC	Not available	Not available	N	0	NA
UPENN-GBM-00307_11	F	57.03	412	Wildtype	Not available	Not available	N	0	NA
UPENN-GBM-00307_21	F	57.28	Not available	Nos/nec	Not available	Not available	Not applicable	91	4
UPENN-GBM-00308_11	M	65.76	205	Wildtype	Not available	90	Y	0	NA
UPENN-GBM-00310_11	F	75.43	75	Wildtype	Methylated	Not available	Y	0	NA
UPENN-GBM-00312_11	M	57.99	334	Wildtype	Unmethylated	Not available	Y	0	NA
UPENN-GBM-00312_21	M	58.72	Not available	Wildtype	Unmethylated	Not available	Not applicable	266	1
UPENN-GBM-00313_11	M	76.94	1723	NOS/NEC	Not available	Not available	N	0	NA
UPENN-GBM-00314_11	M	56.39	Not available	Wildtype	Not available	Not available	Y	0	NA
UPENN-GBM-00314_21	M	58.88	Not available	Wildtype	Unmethylated	Not available	Not applicable	912	3
UPENN-GBM-00315_11	F	70.72	1043	NOS/NEC	Not available	Not available	Y	0	NA
UPENN-GBM-00316_11	M	61.42	98	Wildtype	Unmethylated	Not available	N	0	NA
UPENN-GBM-00317_11	M	84.31	Not available	Wildtype	Not available	Not available	Y	0	NA
UPENN-GBM-00320_11	F	45.62	683	Wildtype	Not available	Not available	Y	0	NA
UPENN-GBM-00320_21	F	46.17	Not available	Wildtype	Not available	Not available	Not applicable	202	3
UPENN-GBM-00322_11	F	33.29	Not available	Wildtype	Not available	Not available	Y	0	NA
UPENN-GBM-00323_11	M	65.26	121	Wildtype	Indeterminate	Not available	N	0	NA
UPENN-GBM-00324_11	M	73.33	185	Wildtype	Not available	Not available	N	0	NA
UPENN-GBM-00325_11	F	65.84	368	Wildtype	Not available	Not available	N	0	NA
UPENN-GBM-00327_11	F	82.16	341	Wildtype	Not available	Not available	Y	0	NA
UPENN-GBM-00328_11	M	57.72	370	Wildtype	Not available	Not available	Y	0	NA
UPENN-GBM-00330_11	M	86.59	74	Wildtype	Not available	Not available	Y	0	NA
UPENN-GBM-00332_11	F	59.47	558	Wildtype	Indeterminate	80	Y	0	NA
UPENN-GBM-00332_21	F	60.7	Not available	Wildtype	Indeterminate	Not available	Not applicable	450	4
UPENN-GBM-00334_11	F	73.05	159	Wildtype	Indeterminate	Not available	Not available	0	NA
UPENN-GBM-00335_11	M	70.83	282	Wildtype	Not available	Not available	N	0	NA
UPENN-GBM-00336_11	F	83.63	13	Wildtype	Unmethylated	70	Y	0	NA
UPENN-GBM-00337_11	M	62.34	385	Wildtype	Not available	Not available	Y	0	NA
UPENN-GBM-00338_11	M	77.86	1483	Wildtype	Not available	Not available	Y	0	NA
UPENN-GBM-00340_11	F	70.82	325	Wildtype	Not available	Not available	N	0	NA
UPENN-GBM-00342_11	F	59.62	60	Wildtype	Indeterminate	Not available	N	0	NA
UPENN-GBM-00344_11	M	70.57	684	Wildtype	Methylated	Not available	Y	0	NA
UPENN-GBM-00345_11	M	58.81	78	Wildtype	Not available	Not available	N	0	NA
UPENN-GBM-00346_11	M	67.23	334	Wildtype	Not available	Not available	Y	0	NA
UPENN-GBM-00348_11	M	80.2	104	Wildtype	Not available	Not available	Y	0	NA
UPENN-GBM-00349_11	M	56.82	149	Wildtype	Not available	80	N	0	NA
UPENN-GBM-00350_11	M	64.78	622	Wildtype	Methylated	80	Not available	0	NA
UPENN-GBM-00351_11	F	62.48	Not available	Wildtype	Methylated	Not available	Y	0	NA
UPENN-GBM-00352_11	M	42.61	617	Wildtype	Unmethylated	90	Y	0	NA
UPENN-GBM-00352_21	M	42.86	Not available	Wildtype	Methylated	Not available	Not applicable	91	4
UPENN-GBM-00353_11	M	61.3	Not available	Wildtype	Not available	Not available	Y	0	NA
UPENN-GBM-00354_11	M	73.4	351	Wildtype	Unmethylated	Not available	Y	0	NA
UPENN-GBM-00354_21	M	74.28	Not available	Wildtype	Indeterminate	Not available	Not applicable	323	4
UPENN-GBM-00355_11	M	66	252	Wildtype	Not available	Not available	N	0	NA
UPENN-GBM-00355_21	M	66.6	Not available	Wildtype	Unmethylated	Not available	Not applicable	221	3
UPENN-GBM-00356_11	M	71.63	996	Wildtype	Methylated	100	N	0	NA
UPENN-GBM-00357_11	F	88	Not available	Wildtype	Indeterminate	Not available	N	0	NA
UPENN-GBM-00358_11	M	83.46	Not available	Wildtype	Methylated	Not available	N	0	NA
UPENN-GBM-00360_11	M	57.19	613	Wildtype	Methylated	Not available	Y	0	NA
UPENN-GBM-00361_11	F	63.87	Not available	Wildtype	Not available	Not available	N	0	NA
UPENN-GBM-00362_11	F	78.09	142	Wildtype	Unmethylated	Not available	Y	0	NA
UPENN-GBM-00363_11	M	65.4	404	Wildtype	Methylated	90	Y	0	NA
UPENN-GBM-00364_11	F	62.63	383	Wildtype	Not available	Not available	Y	0	NA
UPENN-GBM-00365_11	M	33.11	Not available	Mutated	Indeterminate	Not available	Y	0	NA
UPENN-GBM-00366_11	F	71.41	Not available	Wildtype	Not available	Not available	Not available	0	NA
UPENN-GBM-00367_11	M	50.86	538	Wildtype	Unmethylated	Not available	Y	0	NA
UPENN-GBM-00368_11	M	65.34	416	Wildtype	Unmethylated	90	Y	0	NA
UPENN-GBM-00369_11	F	51.75	360	Wildtype	Unmethylated	90	N	0	NA
UPENN-GBM-00370_11	M	68.38	443	Wildtype	Unmethylated	Not available	N	0	NA
UPENN-GBM-00372_11	F	62.16	Not available	Wildtype	Not available	Not available	N	0	NA
UPENN-GBM-00373_11	F	45.54	524	Wildtype	Unmethylated	Not available	Y	0	NA
UPENN-GBM-00374_11	F	66.65	376	Wildtype	Not available	60	N	0	NA
UPENN-GBM-00375_11	F	54.44	319	Wildtype	Unmethylated	Not available	N	0	NA
UPENN-GBM-00376_11	M	63.59	730	Wildtype	Unmethylated	Not available	Y	0	NA
UPENN-GBM-00377_11	F	83.01	589	Wildtype	Methylated	Not available	N	0	NA
UPENN-GBM-00378_11	M	59.92	451	Wildtype	Methylated	Not available	N	0	NA
UPENN-GBM-00379_11	M	59.66	114	Wildtype	Unmethylated	Not available	N	0	NA
UPENN-GBM-00380_11	M	56.37	516	Wildtype	Methylated	Not available	Y	0	NA
UPENN-GBM-00382_11	F	67.73	14	Wildtype	Not available	Not available	Y	0	NA
UPENN-GBM-00384_11	M	63.2	373	Wildtype	Unmethylated	90	Y	0	NA
UPENN-GBM-00385_11	M	57.26	21	Wildtype	Unmethylated	Not available	Y	0	NA
UPENN-GBM-00387_11	M	51.81	455	Wildtype	Unmethylated	90	Y	0	NA
UPENN-GBM-00388_11	M	74.85	1020	Wildtype	Methylated	90	N	0	NA
UPENN-GBM-00389_11	M	67.91	114	Wildtype	Not available	Not available	Y	0	NA
UPENN-GBM-00391_11	M	57.63	93	Wildtype	Unmethylated	90	N	0	NA
UPENN-GBM-00392_11	M	63.43	Not available	Wildtype	Methylated	Not available	N	0	NA
UPENN-GBM-00393_11	F	68.96	336	Wildtype	Unmethylated	Not available	Y	0	NA
UPENN-GBM-00395_11	M	65.52	Not available	Wildtype	Methylated	Not available	N	0	NA
UPENN-GBM-00396_11	M	47.58	Not available	Wildtype	Not available	90	Y	0	NA
UPENN-GBM-00397_11	F	71.55	Not available	Wildtype	Not available	Not available	N	0	NA
UPENN-GBM-00398_11	M	69.36	342	Wildtype	Unmethylated	Not available	Y	0	NA
UPENN-GBM-00399_11	M	60.67	338	Wildtype	Methylated	Not available	Y	0	NA
UPENN-GBM-00403_11	M	68.19	191	Wildtype	Methylated	Not available	N	0	NA
UPENN-GBM-00404_11	M	66.36	688	Wildtype	Methylated	40	Y	0	NA
UPENN-GBM-00405_11	F	66.34	57	Wildtype	Unmethylated	90	Y	0	NA

Table S1 *(continued)*

Table S1 *(continued)*

ID	Gender	Age_at_scan_years	Survival_from_surgery_days	IDH1	MGMT	KPS	GTR_over90percent	Time_since_baseline_preop	PsP_TP_score
UPENN-GBM-00406_11	M	71.33	355	Wildtype	Methylated	90	N	0	NA
UPENN-GBM-00407_11	M	66.52	201	Wildtype	Methylated	Not available	Y	0	NA
UPENN-GBM-00408_11	F	59.47	565	Wildtype	Unmethylated	Not available	Y	0	NA
UPENN-GBM-00409_11	F	72.71	510	Wildtype	Methylated	80	Y	0	NA
UPENN-GBM-00411_11	M	52.12	531	Wildtype	Unmethylated	70	Y	0	NA
UPENN-GBM-00412_11	M	63.11	862	Wildtype	Methylated	100	N	0	NA
UPENN-GBM-00413_11	M	48.47	827	Wildtype	Unmethylated	90	Y	0	NA
UPENN-GBM-00416_11	F	37.53	Not available	Wildtype	Unmethylated	Not available	Y	0	NA
UPENN-GBM-00417_11	F	59.76	1863	Wildtype	Indeterminate	Not available	Y	0	NA
UPENN-GBM-00418_11	F	49.61	1410	Wildtype	Methylated	Not available	Y	0	NA
UPENN-GBM-00419_11	M	59.89	518	Wildtype	Unmethylated	Not available	N	0	NA
UPENN-GBM-00420_11	F	63.36	Not available	Wildtype	Methylated	Not available	Y	0	NA
UPENN-GBM-00421_11	M	60.7	765	Wildtype	Unmethylated	Not available	N	0	NA
UPENN-GBM-00423_11	F	77.45	303	Wildtype	Methylated	Not available	Y	0	NA
UPENN-GBM-00425_11	M	74.89	Not available	Wildtype	Methylated	Not available	N	0	NA
UPENN-GBM-00426_11	M	55.17	820	Wildtype	Unmethylated	90	Y	0	NA
UPENN-GBM-00427_11	F	73.15	136	Wildtype	Not available	Not available	N	0	NA
UPENN-GBM-00428_11	M	64.76	374	Wildtype	Unmethylated	Not available	N	0	NA
UPENN-GBM-00429_11	M	73.66	Not available	Wildtype	Not available	80	N	0	NA
UPENN-GBM-00431_11	F	79.94	125	Wildtype	Unmethylated	Not available	Y	0	NA
UPENN-GBM-00432_11	F	60.63	582	Wildtype	Unmethylated	Not available	Y	0	NA
UPENN-GBM-00433_11	M	45.23	Not available	Wildtype	Not available	Not available	Y	0	NA
UPENN-GBM-00434_11	F	66.18	70	Wildtype	Unmethylated	Not available	N	0	NA
UPENN-GBM-00435_11	F	56.94	205	Wildtype	Unmethylated	Not available	Not Available	0	NA
UPENN-GBM-00436_11	F	67.09	389	Wildtype	Unmethylated	Not available	Y	0	NA
UPENN-GBM-00437_11	F	53.02	82	Wildtype	Indeterminate	Not available	N	0	NA
UPENN-GBM-00439_11	F	47.21	264	Wildtype	Methylated	Not available	N	0	NA
UPENN-GBM-00441_11	M	65.03	619	Wildtype	Not available	Not available	N	0	NA
UPENN-GBM-00442_11	F	80.36	90	Wildtype	Methylated	60	N	0	NA
UPENN-GBM-00443_11	M	78.4	60	Wildtype	Methylated	Not available	N	0	NA
UPENN-GBM-00444_11	M	25.48	Not available	Mutated	Methylated	Not available	Y	0	NA
UPENN-GBM-00445_11	F	60.23	284	Wildtype	Methylated	Not available	Y	0	NA
UPENN-GBM-00446_11	F	67.67	Not available	Wildtype	Methylated	Not available	Y	0	NA
UPENN-GBM-00448_11	M	62.34	288	Wildtype	Unmethylated	Not available	Y	0	NA
UPENN-GBM-00449_11	M	48.97	742	Wildtype	Unmethylated	80	N	0	NA
UPENN-GBM-00451_11	F	64.83	Not available	Wildtype	Indeterminate	Not available	Not available	0	NA
UPENN-GBM-00453_11	M	69.45	Not available	Wildtype	Methylated	Not available	Y	0	NA
UPENN-GBM-00454_11	F	71.65	136	Wildtype	Unmethylated	80	N	0	NA
UPENN-GBM-00455_11	M	60.82	516	Wildtype	Methylated	Not available	N	0	NA
UPENN-GBM-00456_11	M	63.99	149	Wildtype	Unmethylated	Not available	N	0	NA
UPENN-GBM-00457_11	M	66.58	Not available	Wildtype	Unmethylated	Not available	N	0	NA
UPENN-GBM-00458_11	M	57.8	Not available	Wildtype	Unmethylated	Not available	Y	0	NA
UPENN-GBM-00459_11	M	38.9	693	Wildtype	Unmethylated	Not available	Y	0	NA
UPENN-GBM-00460_11	M	61.94	Not available	Wildtype	Unmethylated	Not available	N	0	NA
UPENN-GBM-00461_11	M	64.1	Not available	Wildtype	Methylated	Not available	Y	0	NA
UPENN-GBM-00462_11	F	71.61	Not available	Wildtype	Unmethylated	Not available	Y	0	NA
UPENN-GBM-00463_11	M	65.97	738	Wildtype	Unmethylated	Not available	N	0	NA
UPENN-GBM-00464_11	F	25.57	479	Wildtype	Unmethylated	Not available	Y	0	NA
UPENN-GBM-00465_11	M	58.92	Not available	Wildtype	Not available	Not available	Y	0	NA
UPENN-GBM-00466_11	M	73.59	651	Wildtype	Not available	Not available	Y	0	NA
UPENN-GBM-00467_11	M	55.42	251	Wildtype	Not available	Not available	N	0	NA
UPENN-GBM-00468_11	M	79.32	196	Wildtype	Not available	Not available	Not available	0	NA
UPENN-GBM-00469_11	F	51.54	578	Wildtype	Methylated	Not available	Y	0	NA
UPENN-GBM-00470_11	M	60.59	316	Wildtype	Unmethylated	Not available	Y	0	NA
UPENN-GBM-00471_11	M	69.2	114	Wildtype	Unmethylated	Not available	N	0	NA
UPENN-GBM-00472_11	F	58.86	Not available	Wildtype	Not available	Not available	Y	0	NA
UPENN-GBM-00473_11	F	20.74	36	Wildtype	Unmethylated	Not available	N	0	NA
UPENN-GBM-00475_11	M	62.74	44	Wildtype	Unmethylated	Not available	N	0	NA
UPENN-GBM-00476_11	M	60.63	516	Wildtype	Unmethylated	Not available	Y	0	NA
UPENN-GBM-00477_11	M	55.09	Not available	Wildtype	Not available	Not available	Y	0	NA
UPENN-GBM-00490_11	M	74.58	821	Wildtype	Unmethylated	Not available	Not available	0	NA
UPENN-GBM-00491_11	F	65.25	16	Wildtype	Not available	Not available	Not available	0	NA
UPENN-GBM-00496_11	F	54.26	681	Wildtype	Methylated	Not available	Y	0	NA
UPENN-GBM-00499_11	M	75.08	648	Wildtype	Unmethylated	Not available	N	0	NA
UPENN-GBM-00504_11	M	48.81	Not available	Wildtype	Methylated	Not available	N	0	NA
UPENN-GBM-00508_11	M	56.07	572	Wildtype	Unmethylated	Not available	Not available	0	NA
UPENN-GBM-00510_11	M	76.2	74	Wildtype	Not available	Not available	N	0	NA
UPENN-GBM-00513_11	M	76.86	50	Wildtype	Unmethylated	Not available	N	0	NA
UPENN-GBM-00514_11	M	68.67	1205	Wildtype	Methylated	Not available	Y	0	NA
UPENN-GBM-00516_11	F	58.98	188	Wildtype	Methylated	Not available	N	0	NA
UPENN-GBM-00518_11	M	51.47	Not available	Wildtype	Methylated	Not available	N	0	NA
UPENN-GBM-00519_11	M	32.93	468	Wildtype	Unmethylated	Not available	Y	0	NA
UPENN-GBM-00520_11	M	83.61	122	Wildtype	Methylated	Not available	N	0	NA
UPENN-GBM-00521_11	F	64.21	Not available	Wildtype	Methylated	Not available	Y	0	NA
UPENN-GBM-00523_11	F	60.06	Not available	Wildtype	Unmethylated	Not available	Y	0	NA
UPENN-GBM-00526_11	F	75.19	32	Wildtype	Methylated	Not available	N	0	NA
UPENN-GBM-00527_11	M	71.76	248	Wildtype	Unmethylated	80	N	0	NA
UPENN-GBM-00528_11	M	43.53	598	Wildtype	Unmethylated	Not available	Y	0	NA
UPENN-GBM-00529_11	M	73.05	85	Wildtype	Unmethylated	90	Y	0	NA
UPENN-GBM-00530_11	M	60.66	521	Wildtype	Methylated	Not available	Y	0	NA
UPENN-GBM-00533_11	F	61.89	784	Wildtype	Unmethylated	Not available	Y	0	NA
UPENN-GBM-00534_11	F	61.74	707	Wildtype	Methylated	Not available	N	0	NA
UPENN-GBM-00535_11	F	72.25	215	Wildtype	Unmethylated	60	N	0	NA
UPENN-GBM-00538_11	M	56.26	Not available	Wildtype	Methylated	Not available	Y	0	NA
UPENN-GBM-00539_11	F	61.42	Not available	Wildtype	Methylated	Not available	N	0	NA
UPENN-GBM-00540_11	M	70.81	343	Wildtype	Methylated	Not available	N	0	NA
UPENN-GBM-00541_11	M	52.97	471	Wildtype	Not available	Not available	N	0	NA
UPENN-GBM-00545_11	F	73.72	37	Wildtype	Not available	Not available	N	0	NA
UPENN-GBM-00546_11	M	67.11	127	Wildtype	Methylated	40	N	0	NA
UPENN-GBM-00549_11	F	61.33	490	Wildtype	Unmethylated	90	Y	0	NA
UPENN-GBM-00550_11	M	72.03	166	Wildtype	Not available	Not available	N	0	NA
UPENN-GBM-00551_11	M	71.27	376	Wildtype	Methylated	70	N	0	NA
UPENN-GBM-00552_11	M	78.13	384	Wildtype	Unmethylated	80	N	0	NA
UPENN-GBM-00553_11	F	59.62	Not available	Mutated	Methylated	Not available	N	0	NA
UPENN-GBM-00554_11	M	51.24	376	Wildtype	Methylated	Not available	N	0	NA
UPENN-GBM-00556_11	M	73.05	434	Wildtype	Methylated	Not available	Y	0	NA
UPENN-GBM-00559_11	F	73.32	449	Wildtype	Methylated	Not available	N	0	NA
UPENN-GBM-00560_11	M	67.95	273	Wildtype	Unmethylated	80	N	0	NA
UPENN-GBM-00561_11	F	72.82	80	Wildtype	Indeterminate	Not available	N	0	NA
UPENN-GBM-00564_11	M	36.32	Not available	Mutated	Methylated	Not available	N	0	NA
UPENN-GBM-00565_11	F	58.63	Not available	Wildtype	Methylated	Not available	Not available	0	NA
UPENN-GBM-00566_11	M	67.77	Not available	Wildtype	Methylated	Not available	Y	0	NA
UPENN-GBM-00567_11	M	38.86	Not available	Wildtype	Methylated	Not available	N	0	NA
UPENN-GBM-00568_11	M	71.62	Not available	Wildtype	Methylated	Not available	Y	0	NA
UPENN-GBM-00569_11	M	41.24	Not available	Mutated	Methylated	Not available	N	0	NA
UPENN-GBM-00572_11	F	74.22	104	Wildtype	Unmethylated	90	N	0	NA
UPENN-GBM-00575_11	F	76.93	153	Wildtype	Unmethylated	Not available	Y	0	NA
UPENN-GBM-00576_11	M	87.59	440	Wildtype	Unmethylated	Not available	Y	0	NA
UPENN-GBM-00577_11	F	64.92	Not available	Wildtype	Not available	Not available	Y	0	NA
UPENN-GBM-00578_11	M	67.87	Not available	Wildtype	Methylated	Not available	N	0	NA
UPENN-GBM-00581_11	M	54.63	324	Wildtype	Unmethylated	Not available	Y	0	NA
UPENN-GBM-00582_11	M	78.03	Not available	Wildtype	Not available	80	Y	0	NA
UPENN-GBM-00583_11	M	51.88	123	Wildtype	Unmethylated	Not available	N	0	NA
UPENN-GBM-00588_11	M	61.97	61	Wildtype	Methylated	Not available	N	0	NA
UPENN-GBM-00590_11	F	69.22	297	Wildtype	Unmethylated	90	N	0	NA
UPENN-GBM-00592_11	F	52.33	Not available	Mutated	Methylated	Not available	Y	0	NA
UPENN-GBM-00594_11	M	52.3	Not available	Wildtype	Methylated	80	N	0	NA
UPENN-GBM-00595_11	M	69.12	Not available	Wildtype	Methylated	Not available	Not available	0	NA
UPENN-GBM-00596_11	F	81.95	46	Wildtype	Unmethylated	60	Not available	0	NA
UPENN-GBM-00597_11	F	61.92	381	Wildtype	Unmethylated	Not available	Y	0	NA
UPENN-GBM-00599_11	M	60.01	Not available	Wildtype	Unmethylated	Not available	Y	0	NA
UPENN-GBM-00600_11	M	51.52	Not available	Wildtype	Not available	Not available	Y	0	NA
UPENN-GBM-00601_11	M	59.69	435	Wildtype	Not available	Not available	Y	0	NA
UPENN-GBM-00602_11	M	77.19	252	Wildtype	Methylated	Not available	Not available	0	NA
UPENN-GBM-00604_11	F	62	234	Wildtype	Unmethylated	90	Not available	0	NA
UPENN-GBM-00605_11	M	60.38	Not available	Wildtype	Unmethylated	Not available	Y	0	NA
UPENN-GBM-00606_11	M	58.12	Not available	Wildtype	Methylated	Not available	Y	0	NA
UPENN-GBM-00607_11	F	68.15	Not available	Wildtype	Methylated	Not available	N	0	NA
UPENN-GBM-00608_11	F	79.9	Not available	Wildtype	Methylated	Not available	N	0	NA
UPENN-GBM-00611_11	M	58.09	551	Wildtype	Not available	Not available	N	0	NA

Originally published by the creators of the UPENN-GBM dataset and released under the Creative Commons 4.0 License (1-3). IDH1, Isocitrate dehydrogenase 1 gene; MGMT, O6-methylguanine-DNA-methyltransferase gene; KPS, Karnofsky Performance Score; GTR, Gross Total Resection; PsP_TP_score, Pseudoprogression–True Progression Score; UPENN-GBM, University of Pennsylvania glioblastoma database.

Table S2 Range of acquisition parameters used in selected studies by scanner model

Manufacturer	SIEMENS	SIEMENS	SIEMENS	SIEMENS	SIEMENS	SIEMENS	GE MEDICAL SYSTEMS	SIEMENS	SIEMENS	SIEMENS	SIEMENS	SIEMENS
Scanner Model	TrioTim	Trio	NUMARIS/4	Verio	Espree	Skyra	DISCOVERY MR750w	Avanto	syngo.via.VB10A TrioTim	MAGNETOM Vida	Avanto_fit	Skyra_fit
Magnetic Field Strength	3	2.894	3	3	1.5	3	3	1.5	3	3	1.5	3
T1 Imaging Frequency	123.25–123.257	123.264	123.257	123.203–123.263	63.536–63.548	123.155–123.155	127.744	63.636	123.257	123.256–123.256	63.682	123.259
T1 Repetition Time	400–1760	1620	1760	1730–1760	500–1180	1760	5.536	1180	1760	2200	2200	1760
T1 Echo Time	3.09–4.92	3.87	3.1	3.15–3.21	2.87–17	3.15	1.336	3.11	3.11	2.46	2.96	3.15
T1 Inversion Time	0–950	950	950	900–950	0–600	950	0	600	950	900	900	950
T1 Flip Angle	15–80	15	15	9–15	15–80	15	20	15	15	9	8	15
T1 Pixel Spacing	0.430\0.430–1.094\1.094	0.977\0.977	0.977\0.977	0.488\0.488	0.859\0.859–0.977\0.977	0.488\0.488	0.5273\0.5273	0.488\0.488	0.977\0.977	0.977\0.977	1.016\1.016	0.488\0.488
T1 Slice Thickness	1–4	1	1	0.9–1	1–5	1	1.6	1	1	0.9	1	1
T1GD Imaging Frequency	63.636–123.257	123.257	123.257	123.203–123.263	63.536–123.257	123.155–123.155	127.744	63.636	123.257	123.256–123.256	63.682	123.259
T1GD Repetition Time	1180–1760	1760	1760	1730–1760	1180–1760	1730	5.536	1180	1760	2200	2200	1730
T1GD Echo Time	3.1–3.87	3.87	3.1	3.15–3.21	2.87–3.11	2.75	1.336	3.11	3.11	2.46	2.96	2.75
T1GD Inversion Time	600–950	950	950	900–950	600–950	900	0	600	950	900	900	900
T1GD Flip Angle	15	15	15	9–15	15	9	20	15	15	9	8	9
T1GD Pixel Spacing	0.488\0.488–1.094\1.094	0.977\0.977	0.977\0.977	0.488\0.488–0.527\0.537	0.977\0.977	0.488\0.488	0.5273\0.5273	0.488\0.488	0.977\0.977	0.977\0.977	1.016\1.016	0.488\0.488
T1GD Slice Thickness	1	1	1	0.9–1	1	1	1.6	1	1	0.9	1	1
T2 Imaging Frequency	63.863–123.257	123.264	123.257	123.203–123.263	63.536–63.548	123.155–123.155	127.744	63.636	123.257	123.256–123.256	63.682	123.259
T2 Repetition Time	3200–5340	3500	3200	4680–5410	3630–6880	5410	4000	5150	5340	4710	4040	5410
T2 Echo Time	84–458	354	458	86–89	99–106	90	118.02	102	85	90	89	90
T2 Flip Angle	90–160	180	120	160	180	150	142	150	160	150	150	150
T2 Pixel Spacing	0.469\0.469–1.094\1.094	0.5\0.5	0.897\0.897	0.859\0.859–0.938\0.938	0.430\0.430–0.488\0.488	0.75\0.75	0.430\0.430	0.469\0.469	0.938\0.938	0.75\0.75	0.677\0.677	0.75\0.75
T2 Slice Thickness	0.9–5	1	0.9	3	3–5	3	5	3	3	3	3	3
FLAIR Imaging Frequency	63.636–123.257	123.257	123.257	123.203–123.263	63.536–123.257	123.155–123.155	127.744	63.636	123.257	123.256–123.256	63.682	123.259
FLAIR Repetition Time	8000–15830	9420	9420	9420	9200–10000	10030	10505	10000	9420	10060	9790	10030
FLAIR Echo Time	75–141	140	141	109–111	99–141	137	121.22	93	141	133	87	137
FLAIR Inversion Time	2200–2500	2500	2500	2550	2200–2500	2550	2425.46	2200	2500	2550	2584.6	2550
FLAIR Flip Angle	120–170	170	170	170	150–170	150	111	150	170	150	150	150
FLAIR Pixel Spacing	0.488\0.488–1.094/1.094	0.9375\0.9375	0.9375/0.9375	0.469\0.469–0.527\0.527	0.938\0.938–0.977\0.977	0.938\0.938	1.055\1.055	0.488\0.488	0.938\0.938	0.375\0.375	0.8125\0.8125	0.938\0.938
FLAIR Slice Thickness	3–4	3	3	3	3	3	3	3	3	3	3	3
DTI Imaging Frequency	0–123.257	123.257	123.257	123.203–123.263	0–123.257	123.155–123.155	0	63.636	123.257	123.256–123.256	63.682	123.259
DTI Repetition Time	0–6729	4200	4900	6300–7600	0–5000	5400	0	7500	5000	5400	8000	6200
DTI Echo Time	0–91	83	83	100–106	0–121	95	0	87	86	95	87	95
DTI Flip Angle	0–90	90	90	90	0–90	90	0	90	90	90	90	90
DTI Pixel Spacing	1.719\1.719–2.344\2.344	1.719\1.719	1.719\1.719	1.719\1.719–1.797\1.797	1.719\1.719–1.797\1.797	1.719\1.719–1.875\1.875	None	2.344\2.344	1.719\1.719	1.719\1.719	2.344\2.344	1.719\1.719
DTI Slice Thickness	0–3	3	3	3	0–5	3	0	2.5	3	3	3	3
DSC Imaging Frequency	123.249–123.257	123.257	123.257	123.203–123.263	63.536–123.257	123.155–123.155	127.744	63.636	123.257	123.256–123.256	63.682	123.259
DSC Repetition Time	1740–2000	2000	2000	2000	1440–2000	2000	2000	1700	2000	2000	1700	2000
DSC Echo Time	45–54	45	45	45	45–51.4	45	45	30	45	45	30	45
DSC Flip Angle	35–90	90	90	90	90	90	60	90	90	90	90	90
DSC Pixel Spacing	1.688\1.688–1.953/1.953	1.719\1.719	1.719\1.719	1.719\1.719	1.719\1.719–1.797\1.797	1.719\1.719	1.875\1.875	1.719\1.719	1.719\1.719	1.719\1.719	1.719\1.719	1.719\1.719
DSC Slice Thickness	3–5	3	3	3–5	3–5	4–5	5	5	4	3–4	4	3

Originally published by the creators of the UPENN-GBM dataset and released under the Creative Commons 4.0 License (27-29). T1GD, T1 gadolinium; FLAIR, fluid attenuated inversion recovery; DTI, diffusion tensor imaging; DSC, dynamic susceptibility contrast; UPENN-GBM, University of Pennsylvania glioblastoma database.

https://dx.doi.org/10.21037/qims-23-1471